

# A sensitivity study of vortex breakdown onset to upstream boundary conditions

BENJAMIN LECLAIRE† AND DENIS SIPP

Office National d'Études et de Recherche Aérospatiales (ONERA),  
Department of Fundamental and Experimental Aerodynamics,  
8 rue des Vertugadins, 92190 Meudon, France

(Received 26 March 2008; revised 24 September 2009; accepted 24 September 2009;  
first published online 29 January 2010)

This paper theoretically investigates the influence of the upstream boundary conditions on the bifurcation structure leading to vortex breakdown. The axisymmetric flow of an inviscid fluid in a pipe of constant cross-section and finite axial length is considered. Solutions bifurcating from the columnar solution at criticality are analysed via a weakly nonlinear expansion and computed in the fully nonlinear regime using numerical continuation, until a centreline recirculation is found at the pipe outlet. Bifurcation diagrams are determined for a parametric family of inflows describing a wide range of axial and azimuthal profiles, the third inlet condition being chosen either as a fixed azimuthal vorticity or as a vanishing radial velocity. Including the traditional picture given by Wang & Rusak (*J. Fluid Mech.*, vol. 340, 1997*a*, p. 177), six different diagrams are found to be possible. In particular, a scenario of smooth transition to breakdown may exist as the swirl is increased, with no loss of stability and no hysteresis, breakdown appearing for swirl levels larger than the critical swirl in a pipe. This transition involves a new type of flow akin to a pre-breakdown flow. Our results, furthermore, suggest that rigidly rotating Poiseuille flow could correspond to the limit for which breakdown is impossible because it is predicted at infinitely large swirl numbers. We finally find that flows with a large rotational core are particularly sensitive to an accurate modelling of the upstream boundary conditions, weakly confined vortices being much more robust.

---

## 1. Introduction

Vortex breakdown is a widespread phenomenon that may occur in various natural and technological situations in which rapidly rotating flows with an axial velocity component are involved (e.g. tornadoes, swirl combustors, high-angle-of-attack delta wings), and has therefore motivated important research efforts since its first observation in the late 1950s (Peckham & Atkinson 1957). Even if a universally accepted definition of the phenomenon still seems to be lacking, it is recognized as the abrupt widening of a vortex core, leading to increased unsteadiness and turbulence, and in a majority of cases to a stagnation point on the axis (see, among others, Leibovich 1984; Delery 1994; Althaus, Bruecker & Weimer 1995; Lucca-Negro & O'Doherty 2001 for a review).

Experimental, numerical as well as theoretical studies to date agree that breakdown is mainly controlled by the swirl number  $\omega$  of the flow, which traditionally represents

† Email address for correspondence: benjamin.leclaire@onera.fr

the ratio between the maximum azimuthal velocity and a reference axial velocity at some station of the flow. Breakdown appears as a threshold value  $\omega_1$  is crossed, and in some instances experiences hysteresis, i.e. it may disappear at a value  $\omega_0 < \omega_1$  as the swirl number is progressively decreased from a value larger than  $\omega_1$  (Sarpkaya 1971; Billant, Chomaz & Huerre 1998). Besides, vortex breakdown is known to be highly sensitive to boundary conditions. In various studies, be they experimental or numeric, authors have for instance preferred to consider pipes with a slight divergence or a localized throat (Sarpkaya 1971; Faler & Leibovich 1978; Beran & Culick 1992; Lopez 1994; Buntine & Saffman 1995) in order to prevent vortex breakdown to migrate upstream and reach the vortex generator or the chosen upstream boundary of the pipe. In constant cross-section pipes, steady breakdown bubbles located not directly next to the rotation-imparting device but some distance downstream have also been documented, but their occurrence seems much less frequent (Leibovich 1984; Mattner, Joubert & Chong 2002).

Even if it is experimentally more complex to investigate, vortical flow in a pipe of constant cross-section remains an important case to study. In addition to its practical significance, it is one of the most generic and easily tractable frameworks for the theoretical study of vortex breakdown, as shown by the studies of Leibovich & Kribus (1990) and Wang & Rusak (1997*a*), among others. Rusak and co-workers in particular have explored the bifurcation structure pertaining to the axisymmetric inviscid flow in a straight pipe, encountered as the inflow swirl number  $\omega$  varies (Wang & Rusak 1996*a*, 1996*b*, 1997*a*; Rusak, Wang & Whiting 1998). Their subsequent studies (Rusak, Judd & Wang 1997; Wang & Rusak 1997*b*; Rusak 1998; Rusak & Judd 2001; Rusak & Meder 2004) have envisaged more practically related situations (slight viscosity of the fluid, divergence or convergence of the pipe, or increment of azimuthal vorticity at the inlet) as perturbations from this ‘ideal’ case. Such an approach has provided relevant models consistent with previous experimental and numerical results, helping to understand the transition to breakdown as well as its hysteretical behaviour (see, in particular, Keller, Egli & Exley 1985; Brown & Lopez 1990; Beran & Culick 1992; Lopez 1994; Buntine & Saffman 1995). Note, in particular, that even if vortex breakdown is known as a strongly unsteady and three-dimensional phenomenon, its associated mean flow remains axisymmetric, so that such analyses focusing on the number and properties (including stability) of steady flows in an axisymmetric context have allowed to grasp the major features of its dynamics.

Many of these works aiming at modelling vortex breakdown have also highlighted the choice of upstream boundary conditions as a difficult problem. Simulating numerically an incompressible flow, be it inviscid or viscous, requires to prescribe three conditions at the inlet (see, for instance, Buntine & Saffman 1995), whereas in an experiment, it is not always possible to identify a zone somewhere upstream at which for any swirl number, three radial conditions may be identified, especially if perturbations due to breakdown propagate upstream. A crucial question is thus to know how dependent the scenario leading to breakdown is to one set of upstream boundary conditions, i.e. to assess the sensitivity of breakdown onset to these conditions. This question also has an interest in more favourable situations, in which the upstream propagation is avoided, insofar as numerical or theoretical studies often use simpler profile laws than those measured in the experiments. To our knowledge, a clear theoretical picture on this sensitivity still seems to be lacking. In past studies considering either straight, slightly diverging pipes or pipes with a localized throat, the inlet velocities have been prescribed by mimicking the experimental data in

regimes where no upstream propagation occurs, at least for the azimuthal velocity (Kopecky & Torrance 1973; Grabowski & Berger 1976; Hafez, Kuruvila & Salas 1986; Salas & Kuruvila 1989; Brown & Lopez 1990; Beran & Culick 1992; Lopez 1994; Buntine & Saffman 1995; Rusak 1998; Rusak *et al.* 1998), or by using simplified profiles more tractable for theoretical developments (Keller *et al.* 1985; Goldshtik & Hussain 1997; Gallaire & Chomaz 2004; Gallaire, Chomaz & Huerre 2004). In these works, the third condition has been chosen either as a fixed azimuthal vorticity (in both theoretical and numerical studies) or as a vanishing radial velocity (only in numerical studies). Reviewing these investigations shows, in particular, the existence of two unanswered problems. Firstly, the case of plug axial flow with solid-body rotation appears very paradoxical compared with other inflows such as the q-vortex (See Leibovich 1984, for the definition of the latter flow). While it has been considered in several analyses together with a third condition of zero azimuthal vorticity, and has allowed to complete the theoretical picture of the transition to vortex breakdown (Wang & Rusak 1996a; Gallaire & Chomaz 2004), it is known that this set of conditions also makes the inviscid problem fully linear as long as no recirculation occurs in the flow (see, for instance, Batchelor 1967), which seems contradictory with the strongly nonlinear character of vortex breakdown. In that respect, concerns as to the ability of such a flow to undergo breakdown have already been raised in the past (Kopecky & Torrance 1973; Hanazaki 1996), this question still being unclear. Secondly, the respective influence of the two choices for the third inlet condition has, to our knowledge, never been addressed in a theoretical way. Relying on a review of numerical simulations, Brown & Lopez (1990), Beran & Culick (1992) and Gallaire & Chomaz (2004) have, for instance, reported that no major differences are observed in the flows provided that they have not undergone vortex breakdown. Gallaire & Chomaz (2004) have shown that a condition of vanishing radial velocity instead of a fixed azimuthal vorticity only postpones the loss of stability of a columnar vortex to a slightly higher  $\omega_1$  and that more constraining conditions have to be imposed to completely avoid this instability. In a more general perspective, Snyder & Spall (2000) have even compared flows obtained either by specifying an upstream end at some location downstream of their tube-and-vane apparatus, or by including the whole setup in their numerical domain, and have only observed minor differences between both. Though all these studies have brought supplementary insight in the complex physics of breakdown, they remain qualitative in nature, setup-dependent or only pertain to the linear part of breakdown.

This paper is an attempt to fill in some of these gaps by assessing in a theoretical way the sensitivity of vortex breakdown onset to the upstream boundary conditions. To do so, we choose the model of Wang & Rusak (1997a) and consider the incompressible axisymmetric flow of an inviscid fluid in a pipe of constant cross-section and finite length denoted by  $L$ , which we extend by spanning a large range of possibilities for the inlet conditions. Upon imposing at the pipe inlet a Rankine vortex with plug axial flow, or a q-vortex, together with a fixed azimuthal vorticity, Wang & Rusak (1996a, 1996b, 1997a) have exhibited the bifurcation structure qualitatively sketched in figure 1(a). In this diagram, the axial velocity on the pipe axis at the outlet,  $w(0, L)$ , is represented for all existing flow solutions as a function of  $\omega$ . Three different states are involved in the scenario proposed by Wang, Rusak and their co-workers. The *columnar* solution consists of a flow with no axial gradients. It is stable for low swirl numbers, until the so-called critical swirl in a pipe  $\omega = \omega_1$  is reached, where a transcritical bifurcation occurs, giving birth to a branch where *decelerated* and *accelerated* states are found. This terminology refers to the value of their axial velocity at the centre of the exit

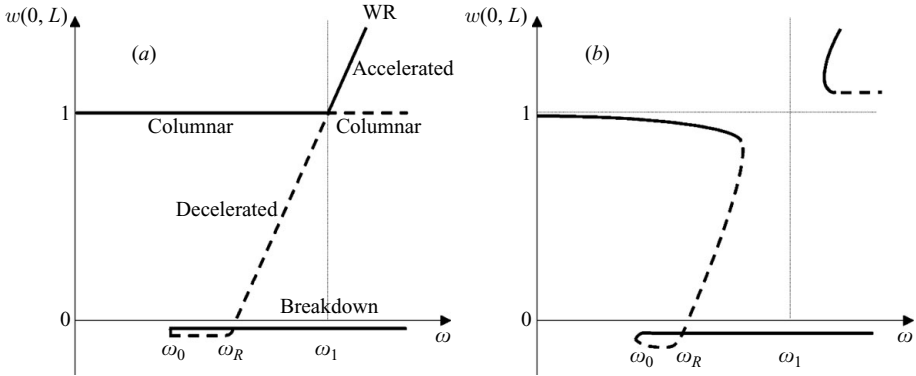


FIGURE 1. Qualitative bifurcation diagrams for the onset of axisymmetric breakdown in a pipe of finite length  $L$ , including branches of stable (solid lines) and unstable (dashed lines) flow solutions. See the text for the definitions of  $\omega_0$ ,  $\omega_R$  and  $\omega_1$ . (a) Inviscid analysis, pipe of constant cross-section (Wang & Rusak 1997a). Notation WR denotes the occurrence of a wall recirculation, as evidenced by Rusak & Meder (2004). (b) Viscous analysis in a pipe with a localized throat (Beran & Culick 1992; Lopez 1994). A similar unfolding of the transcritical bifurcation was also obtained in the framework of an inviscid analysis, for a slightly diverging pipe (Buntine & Saffman 1995; Rusak *et al.* 1997; Rusak & Judd 2001) or a flow with a slight viscosity in a pipe of constant cross-section (Wang & Rusak 1997b).

plane, compared with that of the columnar flow. In this plane, an acceleration on the axis is observed for  $\omega > \omega_1$ , logically accompanied by a deceleration at the wall, and for large enough  $\omega$ , a wall recirculation may be encountered (denoted by WR in figure 1(a), see Rusak & Meder 2004 for the q-vortex and Leclaire, Sipp & Jacquin 2007b for the case of plug axial inflow with solid-body rotation). Such flows are linearly stable. For  $\omega < \omega_1$ , flows are unstable and characterized by a deceleration on the axis that increases as  $\omega$  diminishes from  $\omega_1$ . When the pipe is long, it has been observed that the deceleration is localized near the outlet, with a structure reminiscent of a solitary wave (Leibovich & Kribus 1990; Wang & Rusak 1997a). The limit of a vanishing axial velocity at the centre of the exit section is reached at  $\omega = \omega_R < \omega_1$ . As  $\omega$  further decreases from  $\omega_R$ , this deceleration grows in magnitude so that these flows, which are still unstable, are characterized by a central stagnation zone. As the swirl  $\omega = \omega_0$  is reached, they give birth via a turning point to the stable *breakdown* solutions, which have been shown by Wang & Rusak (1997a) to correspond to the global minimizer of an energy functional for  $\omega > \omega_0$ . According to this analysis, as  $\omega$  is progressively increased from zero, the columnar flow is thus observed until  $\omega_1$ , where it destabilizes and tends to the breakdown solution. The hysteretical behaviour of breakdown is then ascribed to the fact that  $\omega_0 < \omega_1$ . As mentioned above, in a less idealized context, such as when the flow has a slight viscosity (Beran & Culick 1992; Lopez 1994; Wang & Rusak 1997b) or when the pipe has no longer a constant but a slightly divergent cross-section (Buntine & Saffman 1995; Rusak *et al.* 1997; Rusak & Judd 2001), the transcritical bifurcation unfolds, giving rise to two pairs of branches connected by turning points slightly below and above  $\omega_1$ , as sketched in figure 1(b).

In this study, we determine the influence on the accelerated–decelerated branch of the size of the rotational core at the inlet (in a way to encompass both weakly confined vortices and solid-body rotation), of the jet or wake character of the associated axial velocity and of prescribing either a fixed azimuthal vorticity or a vanishing radial velocity at the inlet. We also investigate how the pipe length  $L$  may change the

results. To that aim, we use two different diagnosis tools. First, a weakly nonlinear expansion is derived to compute the slope of the accelerated–decelerated branch at  $\omega = \omega_1$ . Second, numerical continuation is performed to compute the fully nonlinear flows on the part of the accelerated–decelerated branch delimited by flows with a wall or a central recirculation. Using these techniques, new scenarios of transition to breakdown will be exhibited and a detailed investigation will determine for which types of inflows these scenarios are obtained. The synthesis of these results will finally enable to further assess the sensitivity of vortex breakdown onset to the upstream boundary conditions.

The paper is outlined as follows. The flow model is first described in §2, together with its relevance to practical situations and numerical analyses. The investigation techniques are then exposed in §3. The new scenarios of transition to breakdown are described in §4, in which short and long pipes are dealt with separately. The sensitivity analysis is performed in §5, and conclusive remarks are given in §6.

## 2. Flow model

### 2.1. Governing equations

We consider the incompressible axisymmetric flow of an inviscid fluid in a cylindrical pipe of constant radius, taken as the reference length of the problem, and of finite axial length  $L$ . We use cylindrical coordinates  $(r, \theta, z)$ , where  $r$  is the radius,  $\theta$  is the circumferential angle and  $z$  is the axial distance, and the components  $(u, v, w)$  correspond, respectively, to the radial, azimuthal and axial velocities. The flow can be equivalently characterized by the axisymmetric stream function  $\psi$ , which is linked to the velocity via

$$u = -\frac{\psi_z}{r} \quad \text{and} \quad w = \frac{\psi_r}{r}, \quad (2.1)$$

the circulation  $K = rv$  and the reduced azimuthal vorticity  $\chi = (u_z - w_r)/r$ , partial derivatives being herein denoted by a subscript.

With this set of variables, the axisymmetric Euler equations are written in the form

$$K_t + \frac{\psi_r K_z}{r} - \frac{\psi_z K_r}{r} = 0, \quad (2.2a)$$

$$\chi_t + \frac{\psi_r \chi_z}{r} - \frac{\psi_z \chi_r}{r} = \frac{(K^2)_z}{r^4}, \quad (2.2b)$$

$$\chi = -\frac{1}{r^2} \left( \psi_{zz} + \psi_{rr} - \frac{\psi_r}{r} \right), \quad (2.2c)$$

also referred to as the Squire–Long equations. Equations (2.2a) and (2.2b) express, respectively, the conservation of the angular momentum of a fluid particle on its trajectory in the flow and the tilting and stretching of the azimuthal vorticity resulting from a change of curvature of a streamline in a longitudinal plane.

As explained for instance by Buntine & Saffman (1995), this system of equations has to be completed with two boundary conditions on the radial boundaries, with one boundary condition at the outlet and with three at the inlet. Because of axisymmetry and the free-slip condition associated with the assumption of inviscid flow, the axis and the wall must be streamsurfaces of the flow, i.e.

$$\psi(0, z, t) = 0, \quad \psi(1, z, t) = q, \quad (2.3)$$

$q$  denoting the volume flow rate. At the outlet, we choose the flow to be parallel, as has widely been done in the literature (Kopecky & Torrance 1973; Salas & Kuruvila 1989; Brown & Lopez 1990; Lopez 1994; Wang & Rusak 1997a). This leads to

$$\psi_z(r, L, t) = 0. \quad (2.4)$$

At the inlet, the axial and azimuthal velocity components are prescribed via the stream function and circulation

$$\psi(r, 0, t) = \psi_0(r), \quad K(r, 0, t) = \omega K_0(r), \quad (2.5)$$

where  $\omega$  is our inflow swirl number. Condition (2.5) is the first degree of freedom of our analysis, taken by considering a parametric family of functions  $\psi_0$  and  $K_0$ . Note that in the following, we will assume that the inflow has a strictly positive axial velocity, that is,  $\psi_{0r}(r) > 0$  for any  $r$ , and take its value on the axis as the reference velocity, i.e.  $(\psi_{0r}/r)(0) = 1$ . Also,  $K_0(r)$  and  $K_{0r}(r)$  will be here strictly positive functions, since we restrict to centrifugally stable flows (Rayleigh 1916).

Our second degree of freedom consists of considering alternatively the two main possibilities chosen in the literature for the third upstream boundary condition, which are either a fixed azimuthal vorticity or a vanishing radial velocity. These conditions are, respectively, expressed as

$$\psi_{zz}(r, 0, t) = 0 \quad \iff \quad \chi(r, 0, t) = \chi_0(r) \quad (2.6)$$

and

$$\psi_z(r, 0, t) = 0 \quad \iff \quad u(r, 0, t) = 0. \quad (2.7)$$

The quantity  $\chi_0(r)$  refers to the reduced azimuthal vorticity of the parallel inlet flow, that is,

$$\chi_0(r) = -\frac{1}{r^2} (\psi_{0rr} - \psi_{0r}/r). \quad (2.8)$$

Note also that determining a complete bifurcation diagram as in figure 1(a) would require a continuation model to compute breakdown flows or decelerated flows for  $\omega_0 < \omega < \omega_R$ , which all have a stagnation zone (see, for instance, Leibovich & Kribus 1990; Wang & Rusak 1997a and references therein). Such an approach leads to complex developments that are outside the scope of our study. Our numerical analysis will restrict to flows on the accelerated–decelerated branch which keep a strictly positive axial velocity everywhere ( $\psi_r(r, z) > 0$  for any  $(r, z)$ ).

## 2.2. Comments

As described in §1, the assumption of inviscid flow in a pipe of constant cross-section leads to a branching bifurcation at  $\omega = \omega_1$ , which systematically unfolds in a less strict context. This assumption also induces another specificity that it is important to mention, in particular for comparison with the experiments. Compared with the viscous case, it enhances the strength of the outflow boundary, which directly selects the form of the breakdown bubble. Here a parallel flow is enforced via  $\psi_z(r, L) = 0$ . From (2.2), this also implies  $K_z(r, L) = \chi_z(r, L) = 0$ . It is known that this condition leads to recirculation bubbles with an open downstream end (Wang & Rusak 1997a; Rusak *et al.* 1998), while periodic boundary conditions would favour closed bubbles (Leibovich & Kribus 1990). The present choice of a parallel flow is indeed the most physical to us since high Reynolds number flows, which are the natural targets of an inviscid model, more often display open breakdown with a conical shape than closed bubbles, be it in pipes (Sarpkaya 1995) or in jets (Billant *et al.* 1998). Besides,

focusing on one specific bubble geometry is probably not as highly restrictive as it seems, since to date the same scenarios of transition have been retrieved for both open and closed bubbles (compare for instance the works of Beran & Culick 1992 and Wang & Rusak 1997*a*, 1997*b*).

The ability of the above upstream boundary conditions to mimic experiments should also be further commented. For simplicity, we focus on two types of frequently used setups, on which emphasis will be put in the following: swirl vane setups and rotating honeycomb-based setups.

Beginning with situations in which the experimental upstream boundary is free from perturbations related to breakdown, it is known that the flow generated by swirl vanes may be accurately fitted by the q-vortex model, as documented, for instance, by Sarpkaya (1971), Faler & Leibovich (1978) and Mattner *et al.* (2002). Considering a fixed Reynolds number (built on the mean flow rate), the vortex rotational core is usually small with respect to the pipe radius and nearly independent on  $\omega$ , while the axial velocity profile is a jet whose strength increases with  $\omega$  (see, for instance, Faler & Leibovich 1978). In simplified models, such flows have been investigated most often by imposing at the inlet a Burgers–Rott vortex, i.e. a Burgers vortex with superimposed plug axial flow. Together with the third condition chosen either as  $\psi_{zz}(r, 0) = 0$  or as  $\psi_z(r, 0) = 0$ , this has allowed to retrieve the major features of these experiments (Leibovich & Kribus 1990; Beran & Culick 1992; Wang & Rusak 1997*a*). Note that even if  $\psi_z(r, 0) = 0$  may appear more constraining than  $\psi_{zz}(r, 0) = 0$ , the latter allowing the inflow the possibility to have a non-zero radial velocity, both conditions have been equally used in the literature. Also, note that in an inviscid framework (see Buntine & Saffman 1995), these two conditions have different implications on the link between total head  $H$  and circulation  $K$ , and thus on the physical analysis of the flow. More details on this point are given in Appendix B. Directly downstream of a rotating honeycomb on the contrary, it is reasonable to assume that the azimuthal velocity is of the solid-body rotation type, and that condition  $\psi_z(r, 0) = 0$  is enforced due to the fine-celled structure of the honeycomb. Indeed, the only perturbations in radial velocity that may occur in the exit plane of a honeycomb scale with the cell size, which is in all cases one or two orders of magnitude smaller than perturbations linked to breakdown, which scale with the pipe radius. To our knowledge, for such setups there exists, however, no empirical rule nor model regarding the behaviour of the axial velocity profile with increasing  $\omega$ , which seems besides to vary from a facility to the other. For instance, while in Liang & Maxworthy (2005)'s experiment, plug axial flow persists until breakdown appears, we observed in our facility at ONERA a progressive parabolization of the profiles with a velocity excess on the centreline (Leclaire, Jacquin & Sipp 2007*a*), whose origin is still unclear. As far as models are concerned, studies on solid-body rotation to date systematically considered a plug axial flow, as this considerably simplifies the analysis (see, for instance, Wang & Rusak 1996*a*; Gallaire & Chomaz 2004). Note also that these models, as well as the present one, will be most accurate to describe setups in which the pipe downstream of the honeycomb also rotates. When the pipe is fixed (this is the case in Leclaire *et al.* 2007*a*), it is possible that the direct interaction of the highly rotational core with the boundary layer at the pipe wall may lead to a different physics, which is yet to be described and left to future work.

This modelling becomes more difficult in perturbed situations. For swirl vane setups, as mentioned in the literature, it is clear in particular that none of conditions  $\psi_{zz}(r, 0) = 0$  or as  $\psi_z(r, 0) = 0$  can be expected to hold at all times. In the case of a rotating honeycomb on the contrary, the indeterminacy should pertain only

to the axial velocity component, the azimuthal velocity and condition  $\psi_z(r, 0) = 0$  being guaranteed by the constraining organization of the cells. Globally speaking, perturbed cases cannot be described by a unique set of upstream boundary conditions and should thus be expected to be dynamically much more complex. For instance, one may not exclude that the interaction of the perturbations with the inlet result in a loss of steadiness, possibly with an intermittency between several scenarios.

In this analysis, the family of axial and azimuthal velocity profiles injected in (2.5) will include in particular the unperturbed profiles found in the above setups, as well as their related models. Together with the alternative between  $\psi_{zz}(r, 0) = 0$  and  $\psi_z(r, 0) = 0$ , this will highlight in more detail the physical differences between both types of flows, and the repercussions of using simplified upstream boundary conditions in models. In perturbed cases, knowing the different scenarios associated with a large range of possibilities, even if each one pertains to steady states, should at least qualitatively indicate between which kind of ‘limit points’ the expected dynamics could lie.

### 3. Diagnosis tools

#### 3.1. Weakly nonlinear analysis at $\omega = \omega_1$

We here compute the slope  $c = (\partial w(0, L) / \partial \omega)(\omega = \omega_1)$  of the accelerated–decelerated branch at the branching bifurcation when  $\psi_z(r, 0) = 0$  is prescribed. The corresponding value of  $c$  in the alternate case  $\psi_{zz}(r, 0) = 0$  has been derived by Wang & Rusak (1996a) and will be recalled in the course of the analysis for comparison.

##### 3.1.1. The critical swirl in a pipe $\omega_1$

As described by Wang & Rusak (1997a), the *critical swirl in a pipe*  $\omega_1$  is the counterpart for a finite-length pipe of the *critical swirl*  $\omega_B$  first introduced by Squire (1960) and Benjamin (1962). The term critical originally refers to the propagation of the axisymmetric Kelvin waves in a parallel flow with both an axial and a rotating velocity component, that is, a flow with no gradients in the axial direction in an infinitely long pipe. In a steady framework, *supercritical* and *subcritical* flows are distinguished by their respective inability and ability to sustain standing waves. When time-depending solutions are considered, subcritical flows have the property to propagate disturbances both upstream and downstream, while only downstream propagation is possible in supercritical flows. The transition between both regimes occurs at the critical limit  $\omega = \omega_B$ , so that low-swirl flows ( $\omega < \omega_B$ ) are supercritical and high-swirl flows ( $\omega > \omega_B$ ) are subcritical. In the near-critical regime, it is known (see, respectively, Grimshaw 1990; Rusak *et al.* 1997 for examples in unsteady and steady frameworks) that any perturbation in the flow, for instance a geometrical perturbation of the pipe or streamtube, may lead to a resonant excitation of the critical wave and dramatically perturb the columnar flow. As advocated by Wang & Rusak (1997a), in the framework of a *finite-length* pipe, such effects occur—and the flow is then said to be critical—when the swirl number is large enough for a standing wave or a part of it to be trapped in the finite-length pipe. As a result, the *critical swirl in a pipe* is equal to  $\omega_1$ , with  $\omega_1^2 = \omega_B^2 + O(L^{-2})$  so that it tends towards  $\omega_B$  in the limit of an infinite pipe.

##### 3.1.2. Computation of the slope $c$

We consider a generic inflow given by  $\psi_0(r)$  and  $K_0(r)$  close to criticality, i.e. such that  $\omega = \omega_1 + \varepsilon$ , with  $|\varepsilon| \ll 1$ , together with  $\psi_z(r, 0) = 0$ . The flow quantities are then

expressed as perturbations from their counterparts in the columnar flow:

$$\psi(r, z) = \psi_0(r) + \varepsilon\psi_1(r, z) + \varepsilon^2\psi_2(r, z) + \cdots, \quad (3.1a)$$

$$\begin{aligned} K(r, z) &= (\omega_1 + \varepsilon)(K_0(r) + \varepsilon K_1(r, z) + \varepsilon^2 K_2(r, z) + \cdots) \\ &= \omega_1 K_0(r) + \varepsilon(K_0(r) + \omega_1 K_1(r, z)) + \varepsilon^2(K_1(r, z) + \omega_1 K_2(r, z)) + \cdots, \end{aligned} \quad (3.1b)$$

$$\chi(r, z) = \chi_0(r) + \varepsilon\chi_1(r, z) + \varepsilon^2\chi_2(r, z) + \cdots. \quad (3.1c)$$

These expansions are injected in (2.2) and boundary conditions (2.3)–(2.5) and (2.7), making furthermore the assumption of steady flow,  $\partial/\partial t = 0$ . At order  $\varepsilon^0 = 1$ , the obtained equations trivially express that the columnar flow is a solution of the steady motion equations.

At order  $\varepsilon^1$ , we get from (2.2a)

$$\psi_{0r} K_{1z} - K_{0r} \psi_{1z} = 0, \quad \text{so that} \quad K_1 = \frac{K_{0r}}{\psi_{0r}} \psi_1, \quad (3.2)$$

where the assumption of no recirculation in the flow, i.e.  $\psi_{0r} > 0$ , and condition (2.5) have been used after integration in the  $z$  direction. In (2.2b) and (2.2c), the terms of order  $\varepsilon^1$ , respectively, read

$$\psi_{0r} \chi_{1z} - \chi_{0r} \psi_{1z} = 2\omega_1^2 \frac{K_0 K_{1z}}{r^3} \quad \text{and} \quad \chi_1 = -\frac{1}{r^2} \left( \psi_{1zz} + \psi_{1rr} - \frac{\psi_{1r}}{r} \right). \quad (3.3)$$

Upon using (3.2) and integrating in the  $z$  direction, one gets the critical wave equation

$$D^2 \psi_1 + \left( \frac{r^2 \chi_{0r}}{\psi_{0r}} + 2\omega_1^2 \frac{K_0 K_{0r}}{r \psi_{0r}^2} \right) \psi_1 = \psi_{1zz}(r, 0), \quad (3.4)$$

where the notation  $D^2 f = f_{zz} + f_{rr} - f_r/r$  has been introduced and the right-hand side has been determined by the use of condition (2.5) at order  $\varepsilon^1$ . At this point, it is worthwhile emphasizing the existence of this non-trivial right-hand side in (3.4) contrarily to the case  $\psi_{zz}(r, 0) = 0$  (see (3.14)). Since at the inlet  $\psi_1(r, 0) = 0$  from condition (2.5), one obtains  $\psi_{1zz}(r, 0) = -r^2 \chi_1(r, 0)$ . The right-hand side of (3.4) thus expresses the fact that the critical wave has a finite azimuthal vorticity at the inlet, since it is forced to have a vanishing radial velocity there. Equation (3.4) then leads to the following choice for the critical wave  $\psi_1$ :

$$\psi_1(r, z) = \alpha \phi(r) \left( 1 - \cos\left(\frac{\pi z}{L}\right) \right). \quad (3.5)$$

Finally, the equation on  $\phi$  is obtained as

$$r \left( \frac{\phi_r}{r} \right)_r + \left( \frac{r^2 \chi_{0r}}{\psi_{0r}} + 2\omega_1^2 \frac{K_0 K_{0r}}{r \psi_{0r}^2} - \frac{\pi^2}{L^2} \right) \phi = 0. \quad (3.6)$$

At order  $\varepsilon^2$ , using (3.2) and dividing by  $\psi_{0r}$  leads to the following form for (2.2a):

$$K_{2z} = \frac{K_{0r}}{\psi_{0r}} \psi_{2z} + \left( \frac{K_{0r}}{\psi_{0r}} \right)_r \frac{\psi_1 \psi_{1z}}{\psi_{0r}}. \quad (3.7)$$

Using (3.7), (2.2b) then reads

$$\begin{aligned} \psi_{0r} \chi_{2z} - \left( \chi_{0r} + 2\omega_1^2 \frac{K_0 K_{0r}}{r^3 \psi_{0r}} \right) \psi_{2z} &= \psi_{1z} \chi_{1r} - \psi_{1r} \chi_{1z} \\ &+ 2\omega_1^2 \frac{K_0}{r^3 \psi_{0r}} \left( \frac{K_{0r}}{\psi_{0r}} \right)_r \psi_1 \psi_{1z} + 4\omega_1 \frac{K_0 K_{0r}}{r^3 \psi_{0r}} \psi_{1z} + 2\omega_1^2 \frac{K_1 K_{1z}}{r^3}. \end{aligned} \quad (3.8)$$

From (3.3), it can be deduced that

$$\psi_{1z}\chi_{1r} - \psi_{1r}\chi_{1z} = \left( \frac{\chi_{0r}}{\psi_{0r}} + 2\omega_1^2 \frac{K_0 K_{0r}}{r^3 \psi_{0r}^2} \right)_r \psi_1 \psi_{1z} - \left( \frac{\psi_{1,zz}(r, 0)}{r^2} \right)_r \psi_{1z}. \quad (3.9)$$

Using (3.2) again, one thus obtains

$$\begin{aligned} D^2 \psi_{2z} + \left( \frac{r^2 \chi_{0r}}{\psi_{0r}} + 2\omega_1^2 \frac{K_0 K_{0r}}{r \psi_{0r}^2} \right) \psi_{2z} &= \frac{r^2}{\psi_{0r}} \left( \frac{\psi_{1,zz}(r, 0)}{r^2} \right)_r \psi_{1z} \\ - \left( \frac{r^2}{\psi_{0r}} \left( \frac{\chi_{0r}}{\psi_{0r}} + 2\omega_1^2 \frac{K_0 K_{0r}}{r^3 \psi_{0r}^2} \right)_r + 2\omega_1^2 \frac{K_0}{r \psi_{0r}^2} \left( \frac{K_{0r}}{\psi_{0r}} \right)_r + 2\omega_1^2 \frac{K_{0r}^2}{r \psi_{0r}^3} \right) \psi_1 \psi_{1z} &- 4\omega_1 \frac{K_0 K_{0r}}{r \psi_{0r}^2} \psi_{1z}. \end{aligned} \quad (3.10)$$

The amplitude equation is finally obtained by multiplying this equation by  $\psi_{1z}/r$  and integrating on the whole domain. Using the expression of  $\psi_1$  (3.5), one gets after some algebra and integrations by parts:

$$\alpha \left( \frac{\pi^2}{L^2} I_1 + I_2 \right) = -4\omega_1 I_3, \quad (3.11)$$

with the notations

$$I_1 = - \int_0^1 \frac{r}{\psi_{0r}} \left( \frac{\phi(r)}{r^2} \right)_r \phi^2(r) dr, \quad (3.12a)$$

$$I_2 = \int_0^1 \left( \frac{r^2}{\psi_{0r}} \left( \frac{\chi_{0r}}{\psi_{0r}} \right)_r + \frac{2\omega_1^2}{r \psi_{0r}^3} \left[ (K_0^2)_{rr} - \frac{3}{r} (K_0^2)_r \left( 1 - \frac{r^3 \chi_0}{2 \psi_{0r}} \right) \right] \right) \frac{\phi^3(r)}{r} dr, \quad (3.12b)$$

$$I_3 = \int_0^1 \frac{K_0 K_{0r}}{\psi_{0r}^2} \frac{\phi^2(r)}{r^2} dr. \quad (3.12c)$$

Upon retaining terms until the order  $\varepsilon^1$ , the slope  $c$  of the accelerated–decelerated branch at  $\omega = \omega_1$  is finally given by  $c = \partial w(0, L)/\partial \omega = 2\alpha(\phi_r/r)(0)$ .

*Remark.* When condition  $\psi_{zz}(r, 0) = 0$  is used instead of  $\psi_z(r, 0) = 0$ , one obtains (Wang & Rusak 1996b)

$$\alpha I_2 = -4\omega_1 I_3, \quad (3.13)$$

with the same definition of  $I_2$  and  $I_3$  as above, but with different values of  $\omega_1$  and  $\phi$ . As a matter of fact, in that case the critical wave equation reads

$$D^2 \psi_1 + \left( \frac{r^2 \chi_{0r}}{\psi_{0r}} + 2\omega_1^2 \frac{K_0 K_{0r}}{r \psi_{0r}^2} \right) \psi_1 = 0, \quad (3.14)$$

so that  $\psi_1$  has to be chosen under the form

$$\psi_1(r, z) = \alpha \phi(r) \sin \left( \frac{\pi z}{2L} \right) \quad (3.15)$$

and the equation on  $\phi$  becomes

$$r \left( \frac{\phi_r}{r} \right)_r + \left( \frac{r^2 \chi_{0r}}{\psi_{0r}} + 2\omega_1^2 \frac{K_0 K_{0r}}{r \psi_{0r}^2} - \frac{\pi^2}{4L^2} \right) \phi = 0. \quad (3.16)$$

Comparing (3.15) with (3.5), one observes that when  $\psi_{zz}(r, 0) = 0$  is imposed, the critical wave corresponds to the quarter of a wave of length  $4L$ , while it describes the half of a wave of length  $2L$  when  $\psi_z(r, 0) = 0$  is enforced. This is illustrated in

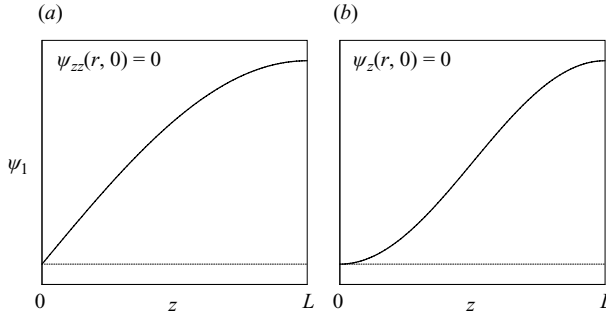


FIGURE 2. Axial evolution of the critical wave  $\psi_1(r, z)$  when  $\psi_{zz}(r, 0) = 0$  (a) or  $\psi_z(r, 0) = 0$  (b) is enforced.

figure 2. A comparison between (3.6) and (3.16) also helps to understand why  $\omega_1$  and  $\phi$  are different in both cases ( $\omega_1$  being slightly higher for  $\psi_z(r, 0) = 0$  as already shown by Gallaire & Chomaz 2004), but that these differences vanish for an infinite pipe length  $L$ .

In practice, in order to compute  $c$  for a precise set of upstream boundary conditions, we first solve eigenproblem (3.6) or (3.16) using a shooting method. For a given value of  $\omega$ , we integrate in  $r$  the wave equation from  $r = 1$  using a fourth-order Runge–Kutta scheme and assuming that  $\phi(1) = 0$  (which stems from the free-slip condition at the wall) and  $\phi_r(1) = -1$ .  $\omega_1$  is obtained when the integration allows to retrieve the proper boundary condition on the axis, that is,  $\phi(0) = 0$ . The quantities  $I_1$ ,  $I_2$ ,  $I_3$ ,  $c$  are then trivially obtained from  $\omega_1$  and  $\phi$ .

### 3.1.3. General remarks

In the following, we will consider instead of  $c$  the quantity

$$\mu = \frac{1}{\omega_1 c}, \quad (3.17)$$

which is built to yield a weakly nonlinear estimate of the value of  $\omega_R$  relatively to  $\omega_1$ . Denoting indeed by  $\omega_R^{wnl}$  the value at which one would obtain  $w(0, L) = 0$  if the accelerated–decelerated branch were approximated by a straight line of slope  $c$ , one has

$$\mu = \frac{\omega_1 - \omega_R^{wnl}}{\omega_1}. \quad (3.18)$$

Using the above analysis, one obtains

$$\mu[\psi_z(r, 0) = 0] = \frac{-\frac{\pi^2}{L^2} I_1 - I_2}{8\omega_1^2 I_3} \frac{1}{(\phi_r/r)(0)}, \quad (3.19a)$$

$$\mu[\psi_{zz}(r, 0) = 0] = -\frac{I_2}{8\omega_1^2 I_3} \frac{1}{(\phi_r/r)(0)}. \quad (3.19b)$$

As  $L$  tends to infinity, quantities  $\omega_1$ ,  $I_1$ ,  $I_2$ ,  $I_3$  and  $(\phi_r/r)(0)$  will be identical for  $\psi_z(r, 0) = 0$  and  $\psi_{zz}(r, 0) = 0$ , and the additional term in  $I_1$  in (3.19a) will vanish. Thus, differences in  $\mu$  stemming from the third inlet boundary conditions will be observed mainly for  $L$  of order unity and vanish for long enough pipes.

The Sturm–Liouville analysis (see in particular Benjamin 1962) shows that  $\phi$  vanishes only for  $r = 0$  and  $r = 1$  and can therefore be taken positive without loss of generality, which implies that  $(\phi_r/r)(0) > 0$ . Besides, the centrifugally stable character

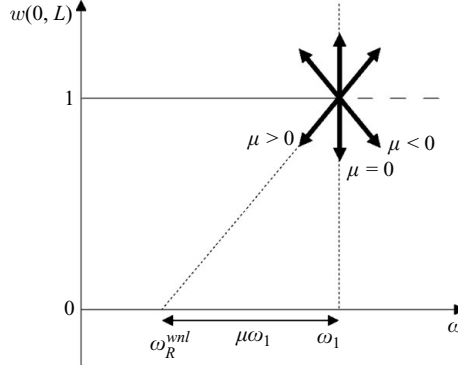


FIGURE 3. Correspondence between the sign of  $\mu$  and the orientation of the accelerated–decelerated branch.

of the inlet flow imposes  $K_{0r}(r) > 0$ , so that  $I_3 > 0$ . Therefore, the sign of  $\mu$  depends only on that of  $-(\pi^2/L^2)I_1 - I_2$  (respectively  $-I_2$ ) in the case  $\psi_z(r, 0) = 0$  (respectively  $\psi_{zz}(r, 0) = 0$ ). For all flows investigated in this study, it is found that  $(\phi(r)/r^2)_r < 0$ , so that  $I_1 > 0$ , since one also has  $\psi_{0r} > 0$ . However, the sign of  $I_2$  will be seen to depend on the choices for  $\psi_0(r)$  and  $K_0(r)$ , making it possible to obtain  $\mu > 0$ ,  $\mu = 0$  or  $\mu < 0$ . The orientations of the decelerated branch corresponding to these three cases are sketched in figure 3. The traditional scenario of Wang & Rusak (1997a) (see figure 1a) thus corresponds to  $\mu > 0$ .

Note also that in the expansion of § 3.1,  $L$  has been implicitly assumed to be of order unity. In the case of long pipes, a multiscale analysis has to be introduced (see, for instance, Leibovich & Kribus 1990; Rusak *et al.* 1997), which is outside the scope of our study. The present weakly nonlinear analysis will thus remain accurate provided that  $\varepsilon \ll L^{-2}$ . It may be used to determine  $c$  irrespective of the pipe length, and its range of accuracy in terms of  $|\omega - \omega_1|$  to describe the branch of accelerated–decelerated flows will be largest for short pipes and smaller for long pipes.

### 3.2. Numerical continuation

#### 3.2.1. Steady solutions

In order to determine exactly the flows far from the bifurcation on the accelerated–decelerated branch, we implemented an algorithm similar to that of Beran & Culick (1992) using the *pseudoarclength continuation* (see, for instance, Keller 1977) and a predictor-corrector scheme based on Newton’s iterations. This technique enables to compute branches of solutions given a guess value at a swirl number  $\omega_{init}$ , even when a turning point is encountered. We refer the interested reader to Beran & Culick (1992) and Govaerts (2000) for more details. The spatial discretization was achieved via a pseudospectral method with Chebyshev polynomials in both the radial and axial directions, and the Fortran LAPACK routines DGETRF and DGETRS were used to perform the matrix inversions.

As sketched in figure 4, the computation of the accelerated–decelerated branch is done via a two-step method that exploits the structural instability of the branching bifurcation at  $\omega = \omega_1$  (this is sometimes referred to as a homotopy method; see, for instance, Govaerts 2000; Kuznetsov 2004):

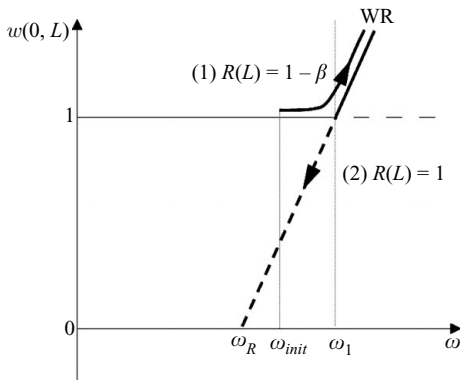


FIGURE 4. Computation of the accelerated–decelerated branch of solutions using a homotopy method.

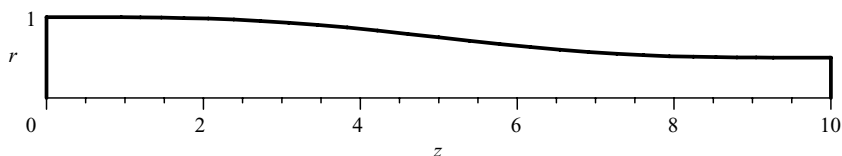


FIGURE 5. Example of converging pipe of radius  $R(z)$  defined by (3.20), here with  $R(L)=0.5$ . Note that in the present method, only a very slight departure of the radius from a constant cross-section was used, i.e.  $R(L)=0.99999$ .

(a) We first deform the computational domain in order to obtain a slightly converging pipe of radius  $R(z)$  given by

$$R(z) = 1 - \beta + \beta \zeta^4 [-20\zeta^3 + 70\zeta^2 - 84\zeta + 35], \quad \zeta = 1 - \frac{z}{L}, \quad 0 \leq z \leq L. \quad (3.20)$$

With such a wall law, the pipe radius  $R(L)$  at the outlet is equal to  $1 - \beta$ . This geometry is sketched in figure 5, where a pipe with exit radius  $R(L)=0.5$  is plotted for clarity. We initialize the branch computation for this geometry by choosing a columnar guess value at  $\omega = \omega_{init}$ . The part of the branch for  $\omega > \omega_{init}$  is computed using the pseudoarclength continuation, until a wall recirculation is obtained in the exit plane. As mentioned in the introduction, the occurrence of this wall recirculation in the exit plane of a slightly converging pipe is a known phenomenon and has been addressed in the cases of the q-vortex (Rusak & Meder 2004) and plug axial flow with solid-body rotation (Leclaire *et al.* 2007b), both these studies using the condition  $\psi_{zz}(r, 0) = 0$ .

In most of the cases studied in this work, we imposed  $\beta = 10^{-5}$  and  $\omega_{init} = 0.95 \omega_1$ , using the value of  $\omega_1$  obtained as described in §3.1.2.

(b) We then return to a constant-cross-section pipe and geometrically deform the flow solution with incipient wall recirculation, which is used as the first guess value. The accelerated–decelerated branch is then computed with the pseudoarclength continuation and an opposite orientation of the tangent vector (see figure 4) until a recirculation is found at the centreline in the exit plane, thereby defining  $\omega_R$ .

### 3.2.2. Stability analysis

The unsteady Squire–Long equations (2.2) may be formally written as

$$\partial_t \mathbf{X} + F(\mathbf{X}) = 0 \quad (3.21)$$

where  $\mathbf{X} = (\psi, K, \chi)$  designates the vector of unknowns and  $F$  is the residual, corresponding to the steady part of the equations. Linear stability consists of monitoring the evolution of small perturbations sought under the form of normal modes,  $\mathbf{X}' = (\psi', K', \chi') = \hat{\mathbf{X}} e^{\sigma t}$ , superimposed on a steady flow  $\mathbf{X}_0$ . Here  $\sigma$  is a complex number, whose real and imaginary parts are respectively the amplification rate and the eigenfrequency of the global mode.  $\mathbf{X}_0$  is thus stable if for all  $\sigma$ ,  $Re(\sigma) < 0$ , unstable if there is any  $\sigma$  such that  $Re(\sigma) > 0$ . Injecting decomposition  $\mathbf{X} = \mathbf{X}_0 + \hat{\mathbf{X}} e^{\sigma t}$  in (3.21) and linearizing, one obtains

$$\sigma \hat{\mathbf{X}} + F_{X_0} \cdot \hat{\mathbf{X}} = 0, \quad (3.22)$$

where  $F_{X_0} = (\partial F / \partial \mathbf{X})_{\mathbf{X} = \mathbf{X}_0}$  denotes the Jacobian of operator  $F$  evaluated for the steady flow  $\mathbf{X}_0$ . The boundary conditions for the stability problem are obtained by linearizing (2.3)–(2.7). They read

$$\psi'(0, z, t) = 0, \quad \psi'(1, z, t) = 0, \quad (3.23)$$

$$\psi'_z(r, L, t) = 0, \quad (3.24)$$

$$\psi'(r, 0, t) = 0, \quad K'(r, 0, t) = 0, \quad (3.25)$$

and for the third upstream boundary condition

$$\chi'(r, 0, t) = 0 \quad (3.26)$$

or

$$\psi'_z(r, 0, t) = 0. \quad (3.27)$$

In the discretization process, as for the steady solutions, (3.22) is transformed into a matrix problem in which these conditions are included. Having obtained a steady flow with Newton's iterations, investigating its stable or unstable character is then quite immediate since the Jacobian  $F_{X_0}$  is computed in the pseudoarclength method. Here for each solution  $\mathbf{X}_0$  obtained by continuation, we determined its eigenspectrum by a direct method, with the Fortran LAPACK routine ZGGEV applied on  $F_{X_0}$ . Note that this is a stability analysis to axisymmetric disturbances only, since (2.2) are axisymmetric. Different results may be found by considering asymmetric perturbations, but this is not the purpose of this study.

Consistent with previous results obtained by Wang & Rusak (1996a,b) and Gallaire & Chomaz (2004), we found that the leading eigenmode, with highest  $Re(\sigma)$ , was always static, i.e. with an eigenfrequency equal to zero. No Hopf bifurcation was found in this study.

## 4. Bifurcation diagrams

In §4.1, we describe our parametric family of inflows. Section 4.2 focuses on the case of a short pipe, of length  $L = 1$ , for two specific inflows. The exploration of the whole set of upstream boundary conditions is led for a longer pipe of length  $L = 10$ , which we think more relevant to experimental situations (§4.3).

#### 4.1. Inlet flows

To build the inlet velocity profiles, we choose the mean axial velocity  $\bar{w}$  (based on the volume flow rate  $q$ ) and the pipe radius  $R_0$  as the reference velocity and length scales. For the velocity in particular, this has been done to facilitate comparisons with the experiments on swirling flows in pipes, in which most often the swirl number is varied, while the Reynolds number based on  $\bar{w}$  is kept nearly constant.

Our profile family is of the q-vortex type. It is defined as

$$\psi_0(r) = \left(1 - \frac{d}{b}\right) \frac{r^2}{2} - \frac{d}{2b} \frac{1 - e^{-br^2}}{1 - e^{-b}}, \quad K_0(r) = \frac{1 - e^{-br^2}}{b}, \quad (4.1)$$

which corresponds to the reduced azimuthal vorticity

$$\chi_0(r) = \frac{2bde^{-br^2}}{1 - e^{-b}} \quad (4.2)$$

and to the velocities

$$w(r, 0) = 1 - \frac{d}{b} + d \frac{e^{-br^2}}{1 - e^{-b}}, \quad v(r, 0) = \frac{\omega}{br} \left(1 - e^{-br^2}\right). \quad (4.3)$$

Figure 6(a) shows examples of these inflows for  $d = 1$ ,  $\omega = 1$  and  $b$  varying from 0 to 10. Note that  $b$  controls the radius  $r_c$  of the rotational core, via  $r_c = 1.12/b^{1/2}$ : large values correspond to a very weak radial confinement and  $b \rightarrow 0$  to solid-body rotation, since in this latter limit

$$w(r, 0) = 1 + \frac{d}{2} - dr^2, \quad v(r, 0) = r. \quad (4.4)$$

This case will hereafter be referred to as  $b = 0$ . Parameter  $d$  is equal to the difference in axial velocity between the centreline and the wall, i.e.  $d = w(0, 0) - w(1, 0)$ : a negative  $d$  corresponds to a wake,  $d = 0$  corresponds to a plug flow and a positive  $d$  corresponds to a jet. As seen from (4.3), (4.4) and figure 6(a), the axial profile is also influenced by  $b$ : as  $b$  decreases from large values, it progressively evolves from a Gaussian towards a parabolic dependence in  $r$ .

Figure 6(b) graphically illustrates the meaning of parameters  $d$  and  $b$ . The shaded zone corresponds to couples  $(d, b)$  for which  $w(r, 0)$  takes vanishing or negative values, which we cannot address in this analysis as explained in §2.1. This figure also locates several inflows labelled I–VI, on which we will focus more specifically in the following.

(a) I is the Burgers–Rott vortex ( $d = 0$  and  $b = 4$ ) studied by Beran & Culick (1992), Lopez (1994) and Wang & Rusak (1997a), among others in order to explain the onset of vortex breakdown in swirl vane setups. Note that in these experiments, flows usually have a smaller rotational core ( $b \approx 10 - 20$ ).

(b) II denotes the plug axial flow with solid-body rotation ( $d = b = 0$ ).

(c) III to V all correspond to axial jets (weak for III, very strong for IV and V) and to moderately or strongly confined vortices; their exact definition in terms of  $d$  and  $b$  is given in table 1 in Appendix A.

(d) VI is a parabolic jet-like axial flow with solid-body rotation ( $d = 1.636$  and  $b = 0$ ). Studying this flow is, in fact, an attempt to tackle the *rigidly rotating Poiseuille flow*, which corresponds to  $d = 2$  and  $b = 0$ , and thus to  $w(0, 1) = 0$ .

For this family of profiles, it is, finally, important to emphasize that the swirl number corresponds to  $\omega = R_0 \Omega(0, 0) / \bar{w}$ , where  $\Omega(r, 0) = v(r, 0) / r$  is the angular velocity in the inlet plane. Denoting  $v_{max}$  the maximum of  $v(r, 0)$  along the radius,  $\omega$  is thus equal to  $v_{max} / \bar{w}$  for  $b = 0$  only, and gets gradually larger than  $v_{max} / \bar{w}$  as  $b$  increases

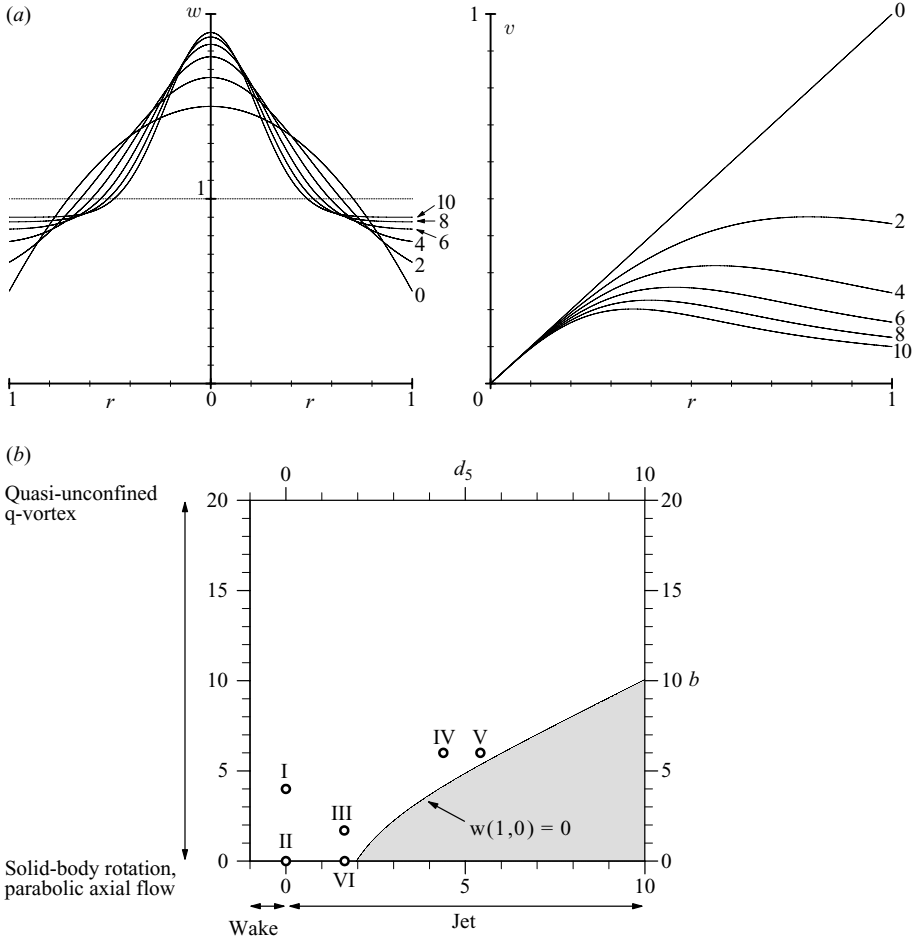


FIGURE 6. Description of the family of inflow profiles.

since at a given  $\omega$ ,  $R_0\Omega(0, 0)$  is the same for all inflows while  $v_{max}$  decreases with  $b$  (see, for example, figure 6a).

### 4.2. Short pipes ( $L = 1$ )

#### 4.2.1. Values of $\omega_1$ and $\mu$

Figures 7 and 8 respectively compare the values of  $\omega_1$  and  $\mu$  in the  $(d, b)$  plane for  $L = 1$  and both cases of the third upstream boundary condition. In the following, we will use label (a) for  $\psi_{zz}(r, 0) = 0$  (left figures) and (b) for  $\psi_z(r, 0) = 0$  (right figures). Consistent with the analysis of §3.1.2, for such a short pipe the values of  $\omega_1$  are higher for  $\psi_z(r, 0) = 0$  than those for  $\psi_{zz}(r, 0) = 0$  for a given profile. However, for both conditions, the same evolutions in the  $(d, b)$  plane are observed. At given  $b$ ,  $\omega_1$  increases with  $d$ , being lowest for wakes and largest for jets, except close to the limit  $w(1, 0) = 0$  where it slightly decreases. At given  $d$ , one observes that  $\omega_1$  increases with  $b$ , and may reach important values for large  $b$ . As mentioned in §4.1, this is a scaling effect since for large  $b$ ,  $\omega$  may become much larger than  $v_{max}/\bar{w}$ .

Figure 8 also shows similar trends for  $\mu$ . It is positive in a large region of the  $(d, b)$  plane, but may also vanish or be negative, indicating the occurrence of

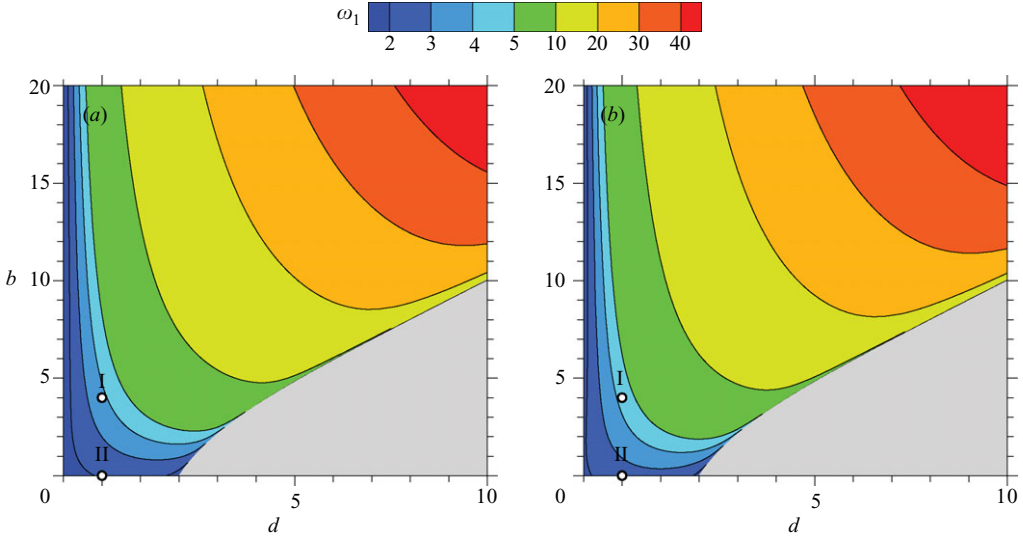


FIGURE 7. Values of the critical swirl  $\omega_1$  as a function of  $d$  and  $b$  for  $L=1$ . (a)  $\psi_{zz}(r, 0)=0$ , (b)  $\psi_z(r, 0)=0$ . I is the Burgers–Rott vortex and II is plug axial flow with solid-body rotation.

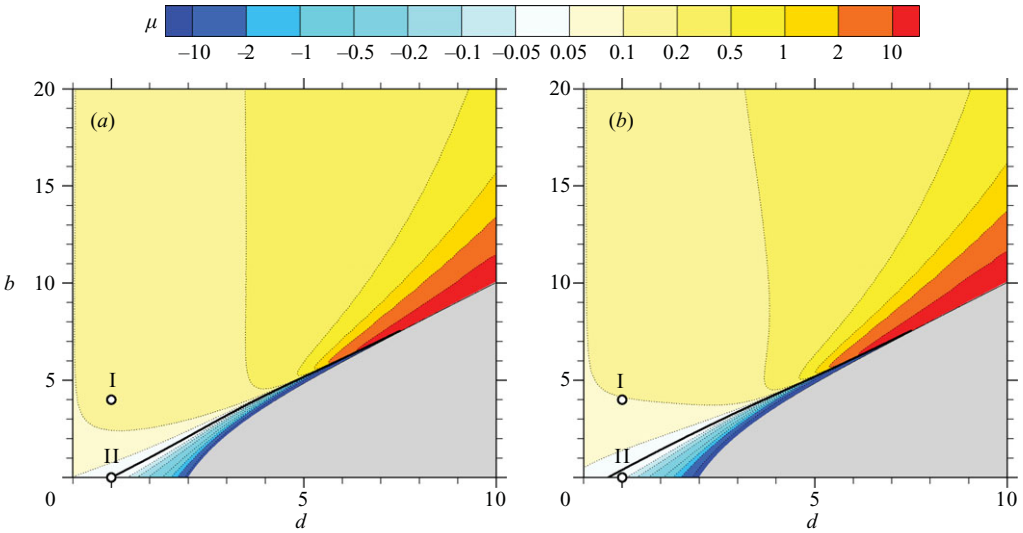


FIGURE 8. Values of  $\mu$  as a function of  $d$  and  $b$  for  $L=1$ . (a)  $\psi_{zz}(r, 0)=0$  and (b)  $\psi_z(r, 0)=0$ . The thick black line denotes the iso-curve  $\mu=0$ .

new bifurcation patterns with an opposite orientation of the accelerated–decelerated branch (see figure 3). Negative values of  $\mu$  are encountered for flows with a large rotational core, relatively close to solid-body rotation, and mainly for jet-like axial flows. More specifically, the smaller  $b$  (below a limit value), the larger the range of  $d$  leading to  $\mu < 0$ . Another global trend for both subcases is the important values of  $|\mu|$  as  $w(1, 0)$  tends towards 0,  $\mu$  being positive or negative depending on  $b$ . Examples of corresponding branches will be given in the case of long pipes. Overall, for this pipe length, the third upstream boundary condition mainly impacts the location of the iso-curve  $\mu = 0$ . For  $\psi_{zz}(r, 0) = 0$ , this curve starts from  $(d, b) = (0, 0)$  so that situations

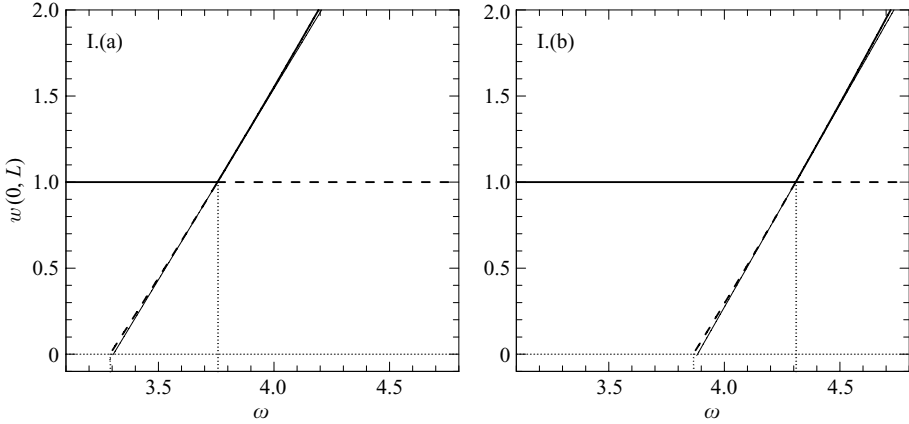


FIGURE 9. Bifurcation diagrams for the Burgers–Rott vortex (I),  $L=1$ . Thick lines are computed branches of solutions (solid if stable, dashed if unstable), the thin solid line is their weakly nonlinear prediction. (a)  $\psi_{zz}(r, 0)=0$ :  $\omega_1=3.756$ ,  $\omega_R=3.290$ ,  $\omega_R^{wnl}=3.305$ . (b)  $\psi_z(r, 0)=0$ :  $\omega_1=4.309$ ,  $\omega_R=3.865$ ,  $\omega_R^{wnl}=3.884$ .

with  $\mu < 0$  only correspond to flows with a jet-like axial profile. For  $\psi_z(r, 0)=0$ , it starts roughly from  $(d, b)=(-0.44, 0)$  so that  $\mu < 0$  also occurs for flows with a wake-like or a plug axial profile. However, these must be very close to solid-body rotation.

#### 4.2.2. Bifurcation diagrams for flows I and II

*I. Burgers–Rott vortex.* Figure 9 shows the branches of solutions obtained for the Burgers–Rott vortex (thick lines) together with their weakly nonlinear prediction (thin lines). Here the accelerated branch was computed only for  $w(0, L) < 2$  and not until a wall recirculation was obtained. We observed that this would have required to run the continuation towards very high swirl numbers and to generate very refined meshes, which we decided to leave to future work.

For  $\psi_z(r, 0)=0$ , we find that the branch orientation of figure 1 is conserved, as well as its stability properties, i.e. stable for  $\omega > \omega_1$  and unstable for  $\omega < \omega_1$ . As shown by comparing the subfigures 9, differences between both choices of the third upstream boundary condition arise here mainly from the difference in  $\omega_1$ , which is more significant than the difference in  $\mu$ ; in these figures, the gap between  $\omega_R$  and  $\omega_1$  has roughly the same magnitude.

It is also interesting to note that a very good agreement is found between the actual flows and their weakly nonlinear prediction, which is *a priori* valid only in the vicinity of  $\omega_1$  and for small departures from a columnar flow. For such a short pipe, even when one approaches  $w(0, L)=0$  at  $\omega_R$ , the departure from the columnar flow remains in fact close to a sinusoidal wave as in the weakly nonlinear expansion of §3.1.2. This may be seen in figure 10, which represents streamlines of flow with incipient recirculation. In this figure, note also the different axial structures obtained for  $\psi_{zz}(r, 0)=0$  and  $\psi_z(r, 0)=0$ , reminiscent of the axial structures of the critical waves  $\psi_1$  sketched in figure 2.

*II. Plug axial flow with solid-body rotation.* Figure 8 shows that for this inflow  $\mu$  may be either vanishing or negative depending on the third condition. Indeed, the

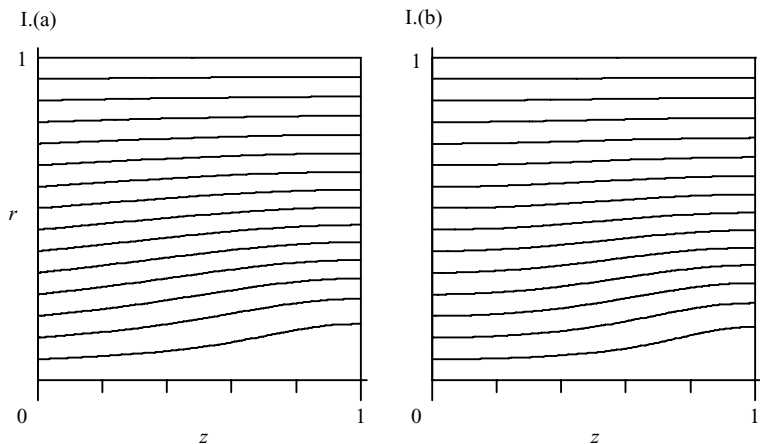


FIGURE 10. Streamlines of flow with incipient recirculation, Burgers–Rott vortex (I),  $L = 1$ . (a)  $\psi_{zz}(r, 0) = 0$ ,  $\omega_R = 3.290$ . (b)  $\psi_z(r, 0) = 0$ ,  $\omega_R = 3.865$ .

integral  $I_2$  in (3.19a) and (3.19b) is zero so that one obtains

$$\mu[\psi_z(r, 0) = 0] = -\frac{\frac{\pi^2}{L^2} I_1}{8\omega_1^2 I_3(\phi_r/r)(0)}, \tag{4.5a}$$

$$\mu[\psi_{zz}(r, 0) = 0] = 0. \tag{4.5b}$$

When  $\psi_{zz}(r, 0) = 0$ , the accelerated–decelerated branch is thus vertical at  $\omega = \omega_1$ . In fact, all elements already exist in the literature to show that the *whole* accelerated–decelerated branch is vertical ( $\omega_R = \omega_1$ ), but to our knowledge this has never been stated as such. With the set of boundary conditions  $\psi_0(r) = r^2/2$ ,  $K_0(r) = r^2$  and  $\psi_{zz}(r, 0) = 0$ , the so-called Bragg–Hawthorne equation, which is equivalent to the Squire–Long equations in the steady case, becomes *linear* (see Batchelor 1967, and Appendix B, for more details). As a result it is possible to derive a perturbation expansion similar to that of § 3.1, but with a perturbation that can be taken of order unity instead of infinitesimal (see, for instance, Grimshaw & Yi 1993; Leclaire *et al.* 2007b). Consequently, at  $\omega = \omega_1$ , perturbations of arbitrarily large amplitude may be superimposed on the columnar flow, i.e. large enough for  $w(0, L)$  to vanish, so that  $\omega_R = \omega_1$ . When a stagnation model is introduced and solutions with closed streamlines are explored, the resulting problem however becomes nonlinear again (see for instance Keller *et al.* 1985).

The accelerated–decelerated branch is no longer vertical but oriented in the direction  $\mu < 0$  when condition  $\psi_z(r, 0) = 0$  is enforced. Figure 11 shows the complete branches obtained by numerical continuation. Consistent with this new orientation, flows on the accelerated–decelerated branch are now *unstable* for  $\omega < \omega_1$  and *stable* for  $\omega > \omega_1$ . As discussed in § 2.2, this new truly nonlinear diagram with  $\psi_z(r, 0) = 0$  should be the natural bifurcation portrait associated with plug axial flow with solid-body rotation in short pipes, since such flows are generated experimentally via a rotating honeycomb.

### 4.3. Long pipes ( $L = 10$ )

#### 4.3.1. Values of $\omega_1$ and $\mu$

In the same way as for short pipes, figures 12 and 13 respectively represent isocontours of  $\omega_1$  and  $\mu$  in the  $(d, b)$  plane for  $L = 10$ . In figure 12, we only show the case  $\psi_{zz}(r, 0) = 0$  since the plot for  $\psi_z(r, 0) = 0$  is quasi-identical. For both figures 12

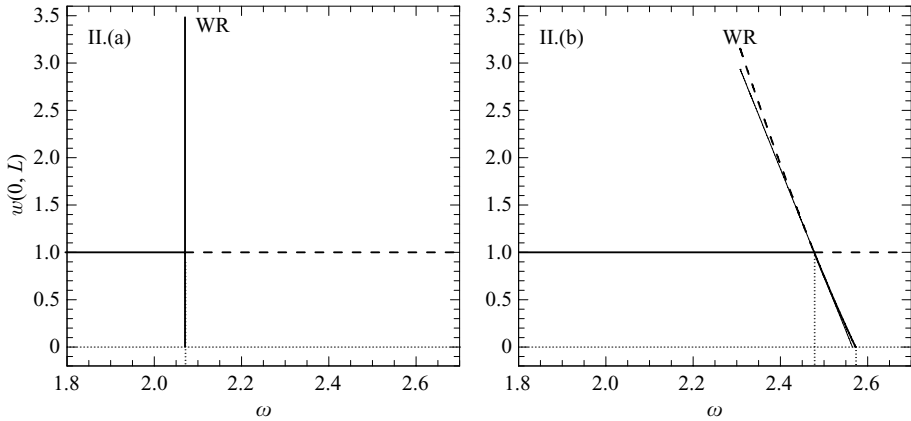


FIGURE 11. Bifurcation diagrams for plug axial flow with solid-body rotation (II) with  $L = 1$ . Thick lines are computed branches of solutions (solid if stable, dashed if unstable), the thin solid line is their weakly nonlinear prediction. (a)  $\psi_{zz}(r, 0) = 0$ :  $\omega_1 = \omega_R = \omega_R^{wnl} = 2.071$ . (b)  $\psi_z(r, 0) = 0$ :  $\omega_1 = 2.478$ ,  $\omega_R = 2.572$ ,  $\omega_R^{wnl} = 2.565$ . Notation WR indicates the occurrence of a wall recirculation in the exit plane.

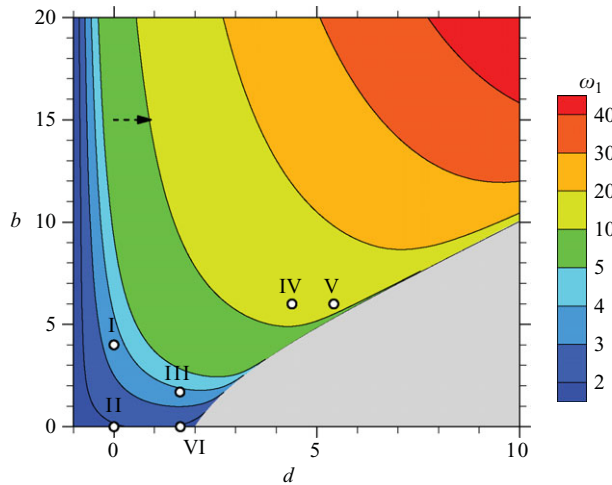


FIGURE 12. Values of  $\omega_1$  as a function of  $d$  and  $b$ ,  $L = 10$ ,  $\psi_{zz}(r, 0) = 0$ . A quasi-identical plot is obtained for  $\psi_z(r, 0) = 0$ . Inflows I–VI are introduced in §4.1. The dashed arrow sketches the qualitative evolution of the upstream velocity profiles in a swirl vane setup such as that of Faler & Leibovich (1978) as  $\omega$  increases towards  $\omega_1$  (as commented in §5).

and 13, the same global trends as for  $L = 1$  are retrieved; the reader is thus referred to the previous paragraph for a more complete description. In the same way as for  $\omega_1$ , figure 13 confirms the progressive convergence with  $L$  of  $\mu[\psi_{zz}(r, 0) = 0]$  and  $\mu[\psi_z(r, 0) = 0]$  towards the same values, except for the zones associated with largest values of  $|\mu|$  where discrepancies are noticed and a larger  $L$  would be required. In particular, the iso-curve  $\mu = 0$  now has exactly the same location in both plots.

We will show below that even if the weakly nonlinear theory does not show any difference for the two boundary conditions for  $L = 10$ , the bifurcation diagrams may strongly depend on the chosen one far enough from  $\omega = \omega_1$ .

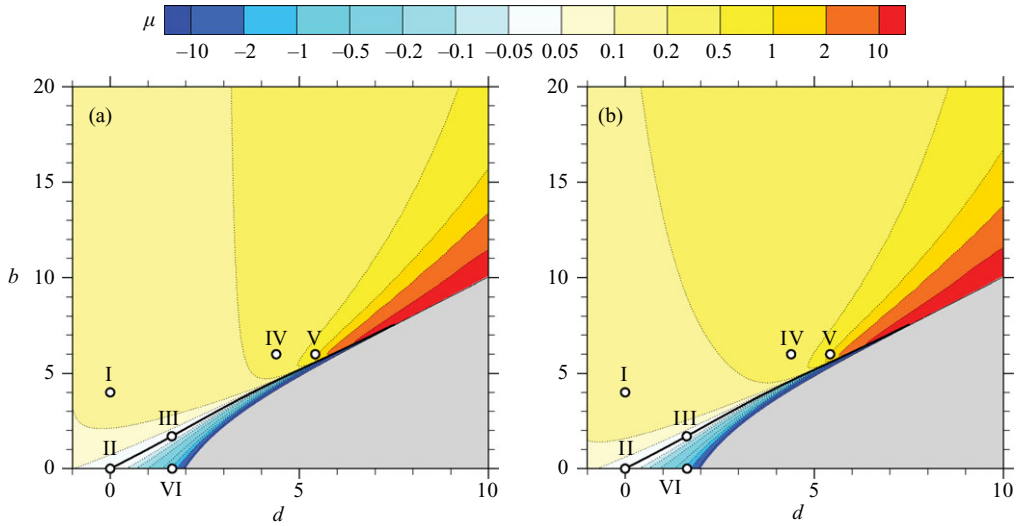


FIGURE 13. Values of  $\mu$  as a function of  $d$  and  $b$  for  $L = 10$ . (a)  $\psi_{zz}(r, 0) = 0$ , (b)  $\psi_z(r, 0) = 0$ . The thick black line denotes the iso-curve  $\mu = 0$ .

#### 4.3.2. Bifurcation diagrams

As seen in figure 13, inflows I, IV and V are characterized by  $\mu > 0$ , II and III by  $\mu = 0$  or  $\mu \approx 0$  and VI by  $\mu < 0$ . Each of these inflows is in fact an example of the six possible bifurcation diagrams for  $L = 10$ . These diagrams are shown in figures 14 and 15. Similar to the case  $L = 1$ , label (a) stands for  $\psi_{zz}(r, 0) = 0$  (left figures) and (b) stands for  $\psi_z(r, 0) = 0$  (right figures), and thin lines denote the weakly nonlinear prediction. For each inflow, we also plot streamlines of the flows with incipient recirculation in the exit plane, corresponding to  $\omega = \omega_R$  (figures 16 and 17). Numerical values of the swirl thresholds corresponding to figures 14–17 can be found in table 1 of Appendix A.

For the Burgers–Rott vortex (I), compared with  $L = 1$ , there remains almost no difference between subcases (a) and (b): decelerated branches are nearly identical, as well as the values of  $\omega_R$ , as shown by figure 14. Another difference with  $L = 1$  is that flows on this branch are now sinusoidal waves only very close to the transcritical bifurcation, since the weakly nonlinear prediction is tangent to the decelerated branch only in the very near vicinity of  $\omega = \omega_1$ . Note that in all other cases as well, flows are logically of the sinusoidal wave type very close to  $\omega = \omega_1$ ; this is not indicated in the figures for clarity. Far enough from this bifurcation, *solitary wave* flows are encountered instead, as described by Wang & Rusak (1997a) for case I.(a). Examples of such flows can be seen in figure 16 at  $\omega = \omega_R$ . These flows are indeed parallel except in the near vicinity of the outlet, where a localized swelling is observed. The same stability properties as those for  $L = 1$  are retrieved as expected.

Consistent with figure 13, one observes in figure 14 that in case II.(b), the decelerated branch is now nearly vertical. Note the very refined scale on the  $x$  axis on these diagrams. As predicted by (4.5a), this branch would be rigorously vertical for an infinite  $L$ . Whatever the third upstream boundary condition, flows associated with II remain of the sinusoidal wave type on the whole decelerated branch, as seen in figure 16, and are stable, as for  $L = 1$ . All these conclusions also pertain to inflows III.(a) and (b), which are examples of–very mildly–supercritical pitchforks. Note that

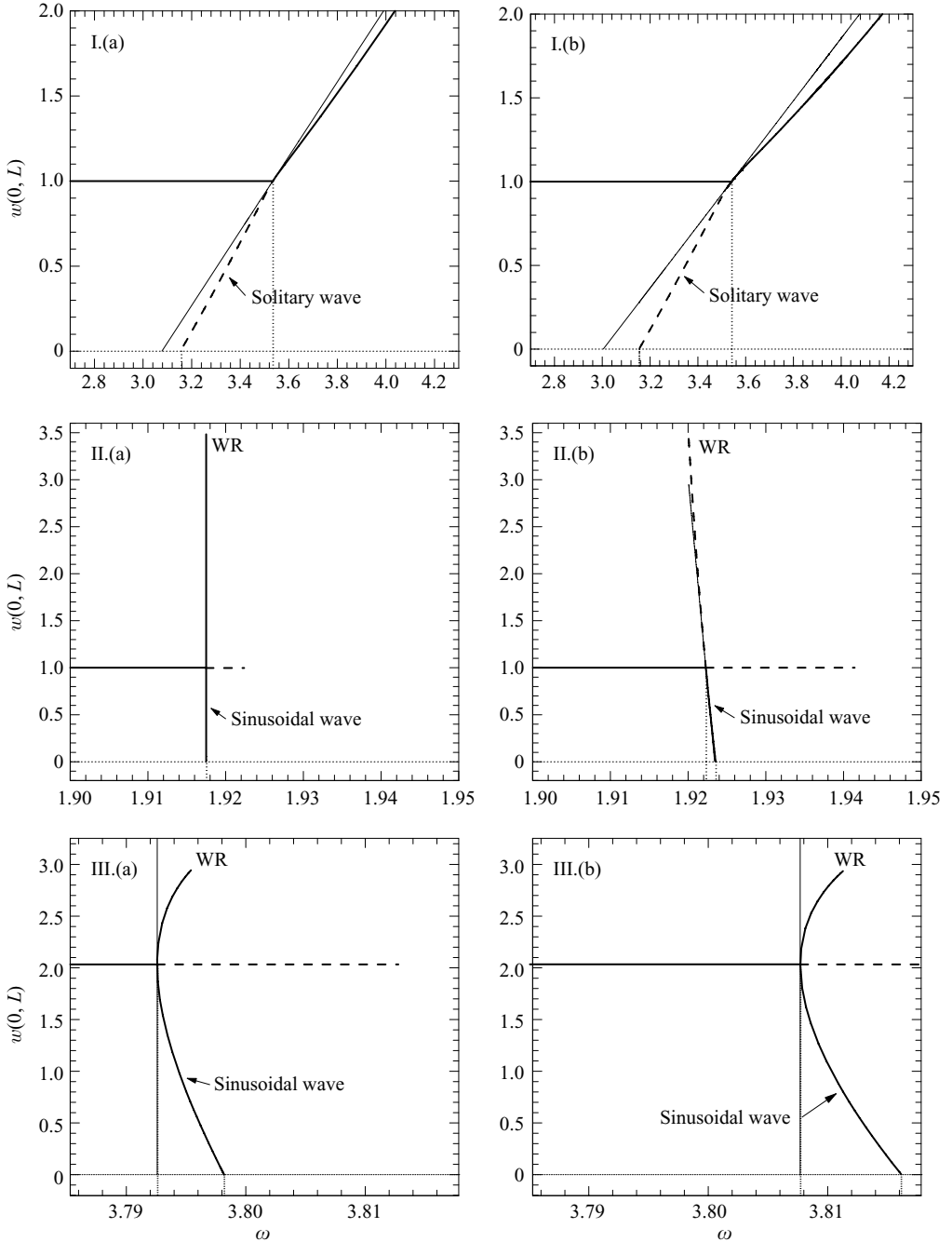


FIGURE 14. Bifurcation diagrams obtained for inflows I(a)–III(b),  $L = 10$ . Thick black lines are computed branches of solutions (solid if stable, dashed if unstable), the solid thin line is their weakly nonlinear prediction. The unstable part of the columnar branch is plotted only until a second branching bifurcation is encountered. This may occur for swirl levels very close to  $\omega_1$ . Numerical values are gathered in table 1 in Appendix A.

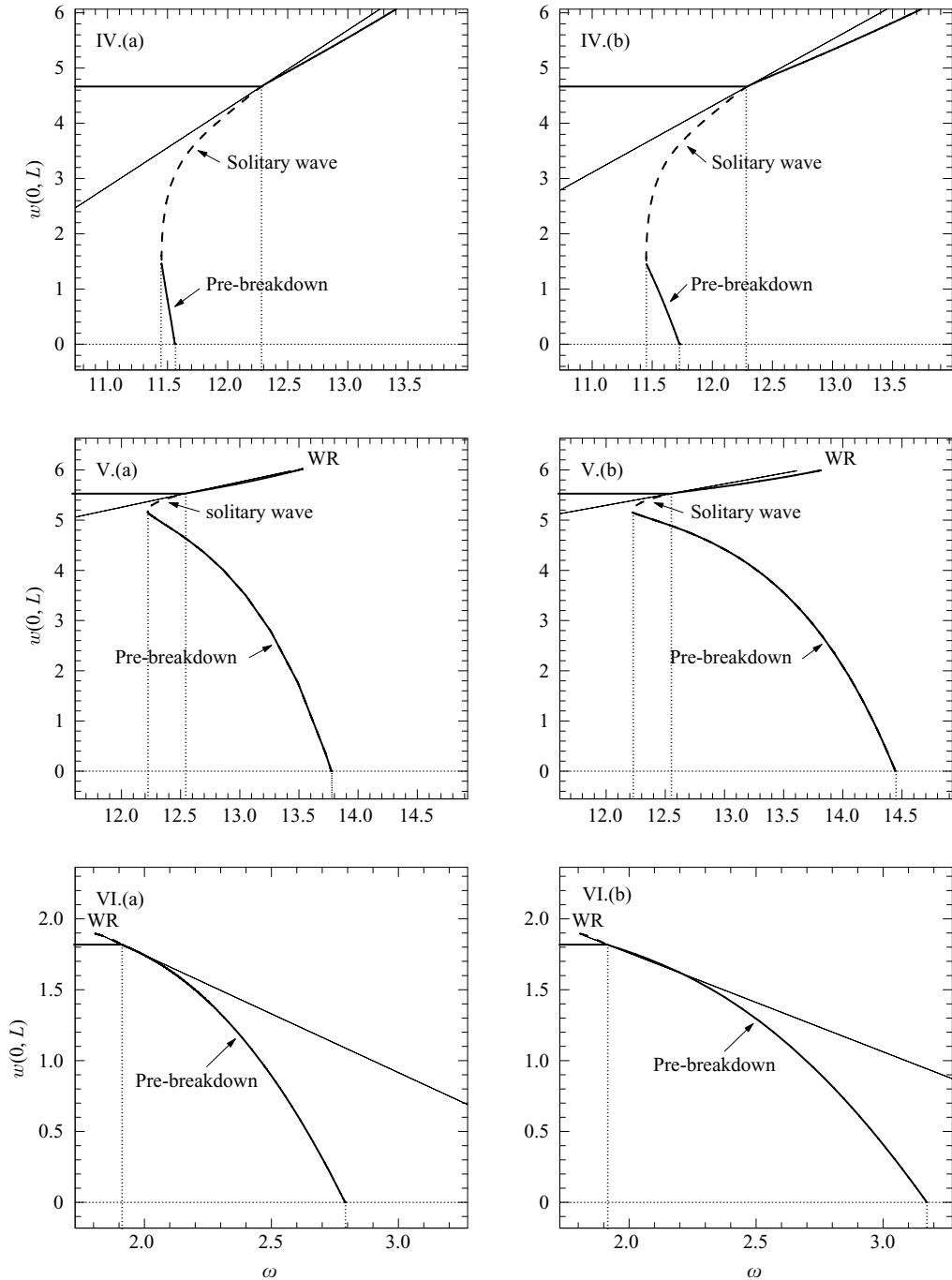


FIGURE 15. Bifurcation diagrams obtained for inflows IV.(a)–VI.(b),  $L = 10$ . Thick black lines are computed branches of solutions (solid if stable, dashed if unstable), the solid thin line their weakly nonlinear prediction. The unstable part of the columnar branch is plotted only until a second branching bifurcation is encountered. This occurs here for swirl levels very close to  $\omega_1$ . Numerical values are gathered in table 1 in Appendix A.

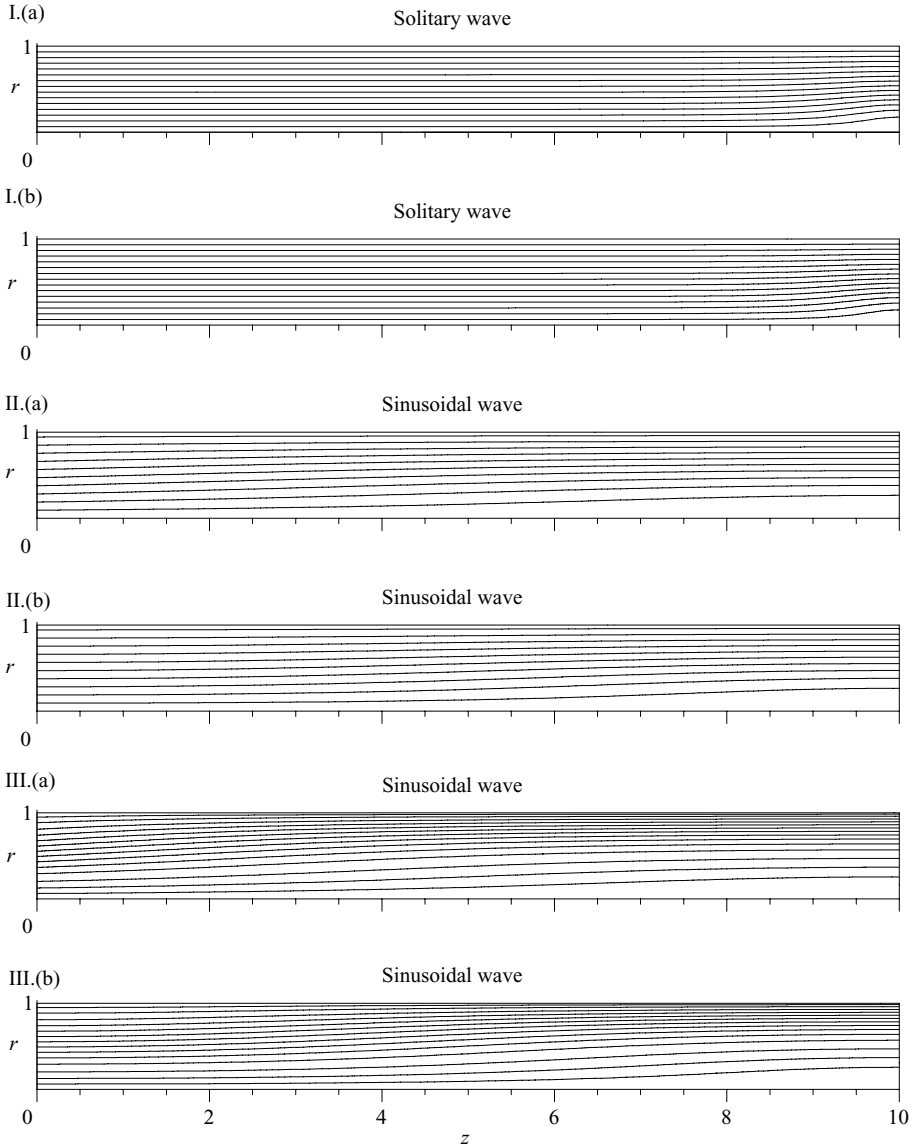


FIGURE 16. Streamlines of flows with incipient recirculation ( $\omega = \omega_R$ ), inflows I.(a)–III.(b). See table 1 in Appendix A for the numerical values of  $\omega_R$ .

for these latter inflows, the values of  $d$  and  $b$  had to be chosen slightly differently according to the subcase in order to have a pitchfork in both (see table 1 in Appendix A). As seen in figure 16, all the sinusoidal wave flows have indeed the same smooth axial evolution as that appearing in figure 10.

Cases IV.(a)–VI.(b) involve a totally new type of flow, which we termed *pre-breakdown*, and which is linearly stable. In this flow, the axial gradients are concentrated exclusively upstream, since it consists of a perturbation directly ‘glued’ to the inlet connected to a quasi-parallel flow downstream. This may be seen in any of the subfigures 17, with a more or less dramatic perturbation close to the inlet. This flow is in some way symmetrical to the solitary wave, in which the perturbations are

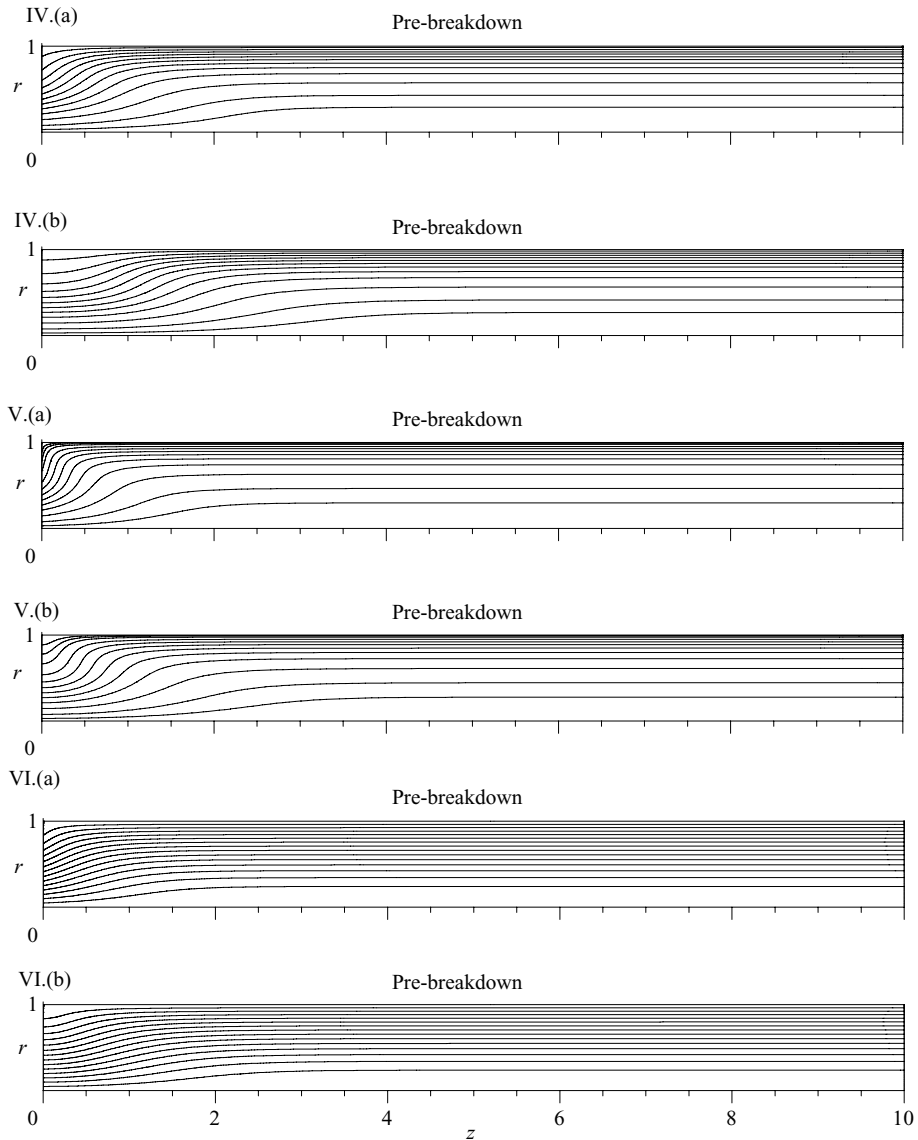


FIGURE 17. Streamlines of flows with incipient recirculation ( $\omega = \omega_R$ ), inflows IV.(a)–VI.(b). See table 1 in Appendix A for the numerical values of  $\omega_R$ .

glued to the outlet. As shown by figure 15, what distinguishes diagrams IV to VI is that for IV and V, the decelerated branch consists of a branch of solitary waves and of a branch of pre-breakdown flows connected by a turning point at a swirl  $\omega_2$ , while in case VI, the decelerated branch consists only of pre-breakdown flows. Cases IV and V besides differ by the order of  $\omega_1$  and  $\omega_R$ , namely  $\omega_R < \omega_1$  for IV and  $\omega_R > \omega_1$  for V. Figure 18 shows the streamlines of three flows (solitary, intermediate and pre-breakdown) encountered on the decelerated branch of IV.(a) around the turning point at  $\omega = \omega_2$ .

Case VI is maybe the most remarkable of these new bifurcation diagrams. It is characterized by a strongly negative  $\mu$ , so that only pre-breakdown flows are observed

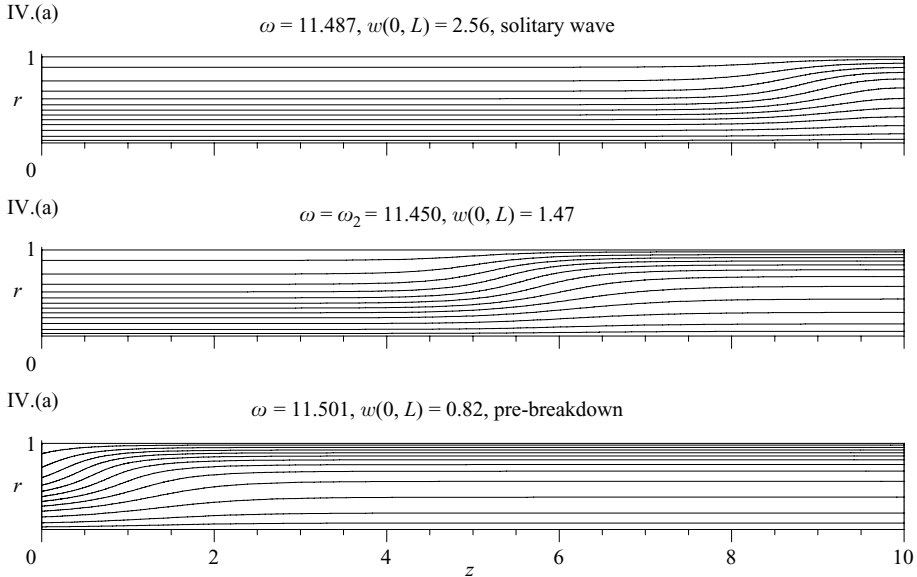


FIGURE 18. Streamlines of flows, case IV.(a), selected values of  $\omega$  near the turning point at  $\omega_2$ .

and  $\omega_R > \omega_1$ . In fact, it corresponds to the largest positive value of  $\omega_R - \omega_1$  relative to  $\omega_1$  among the cases addressed here. As mentioned in §4.1, we consider this case as an intermediate step towards the rigidly rotating Poiseuille flow  $(d, b) = (2, 0)$ . It is very interesting to observe that from figure 13,  $\mu$  should tend to  $-\infty$  for this inflow, and thus  $\omega_R$  to  $+\infty$ , making any occurrence of vortex breakdown impossible. To us, this is a new and important conjecture, which naturally calls for an extension to viscous flows in future works.

The relevance of the weakly nonlinear analysis to describe all these flows directly follows from their type. Upon comparing the positions of the thick and thin lines in the diagrams of figures 14 and 15, one observes that excellent agreement is logically found for the sinusoidal wave flows (cases II and III), which have the same axial evolution as that in the weakly nonlinear analysis. Note that this is also consistent with the fact that the corresponding accelerated–decelerated branches are nearly vertical, i.e. characterized by weak values of  $\omega - \omega_1$ . On the contrary, the agreement is poorer with solitary wave flows (cases I, IV and V), and almost nonexistent with pre-breakdown flows far enough from criticality (IV–VI).

The difference between these flow structures also explains the influence, if any, of the third upstream boundary condition on the bifurcation diagrams. As a matter of fact, it has nearly no impact on the solitary and sinusoidal wave flows, which have weak axial gradients near the inlet, whereas a strong influence is observed on the pre-breakdown flows, which directly interact with the inlet and therefore differ according to the third upstream boundary condition (see figures 16 and 17 and the repercussions on the bifurcation diagrams in figures 14 and 15). In case I, note that this lack of sensitivity agrees with the qualitative conclusions drawn, for instance, by Beran & Culick (1992) or Gallaire & Chomaz (2004), which are based upon a review of several numerical studies. These authors observed that imposing one condition or the other leads to no major differences provided that no recirculation occurs in the flow.

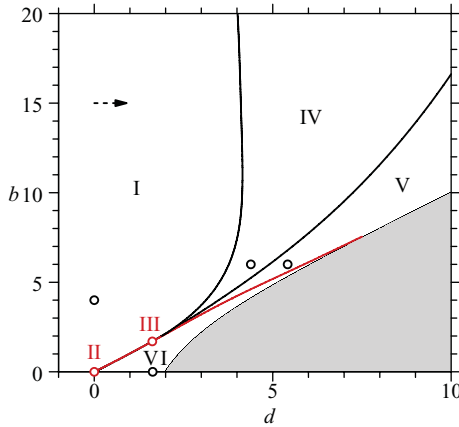


FIGURE 19. Location of the bifurcation diagrams in the  $(d, b)$  plane,  $L = 10$ ,  $\psi_{zz}(r, 0) = 0$ . The analysis leading to this figure, which is specific to the case  $\psi_{zz}(r, 0) = 0$ , is detailed in Appendix C. The red line is the iso-line  $\mu = 0$ . The dashed arrow sketches the qualitative evolution of the upstream velocity profiles in a swirl vane setup such as that of Faler & Leibovich (1978) as  $\omega$  increases towards  $\omega_1$  (as commented in § 5).

To conclude, we plot in figure 19 the delineations showing where each diagram I to VI prevails in the  $(d, b)$  plane, for  $\psi_{zz}(r, 0) = 0$ . As tracing the decelerated branches for all flows in this plane and for both  $\psi_{zz}(r, 0) = 0$  and  $\psi_z(r, 0) = 0$  would not have been realistic, we used here an additional analysis, which is valid for  $\psi_{zz}(r, 0) = 0$  only. Its physical principle and numerical implementation are detailed in Appendix C. Figure 19 shows that pre-breakdown flows and the new bifurcation diagrams IV–VI are encountered only for axial inflows of the jet type, but that different jet strengths are required for them to appear depending on the size of the rotational core. For weakly confined vortices (moderate to large  $b$ ), only the jets with a very high strength ( $d > 3$ ) lead to one of these diagrams, which is then most probably IV or V, while in the limit of solid-body rotation ( $b = 0$ ) any axial profile with a velocity excess on the axis ( $d \geq 0$ ) leads to VI. Note that in the case  $\psi_z(r, 0) = 0$ , the red line (iso-line  $\mu = 0$ ) will have nearly the same location, as shown by figure 13. On the contrary, the locations of the separation lines between I and IV on the one hand, and IV and V on the other hand, will probably differ.

#### 4.3.3. *Examples of unfoldings for a slightly diverging pipe*

As mentioned in the introduction, any perturbation from the model of inviscid flow in a straight pipe leads to the unfolding of the branching bifurcation at  $\omega = \omega_1$ . For the new diagrams described above, we found that a slight pipe divergence has the same effect as that evidenced by Buntine & Saffman (1995) and Rusak *et al.* (1997) for case I.(a). We plot in figure 20 examples for cases IV.(a) and VI.(a) and slightly diverging pipes, with  $R(L) = 1.01, 1.1$  and  $1.2$ , and still  $L = 10$ .

In case IV.(a), the transcritical bifurcation indeed unfolds as a turning point around  $\omega_1$ . Since there is also a turning point near  $\omega_2$ , this means that as  $\omega$  is increased from a low value, the columnar flow will be destabilized at a given swirl close to  $\omega_1$ , and that depending on the value of  $R(L)$ , the flow will either converge towards a stable pre-breakdown state and then gradually evolve towards a stable breakdown state as the swirl is increased again (here, this is encountered for  $R(L) \geq 1.1$ ), or it will converge towards a breakdown state after it is destabilized near  $\omega_1$  (here, this is

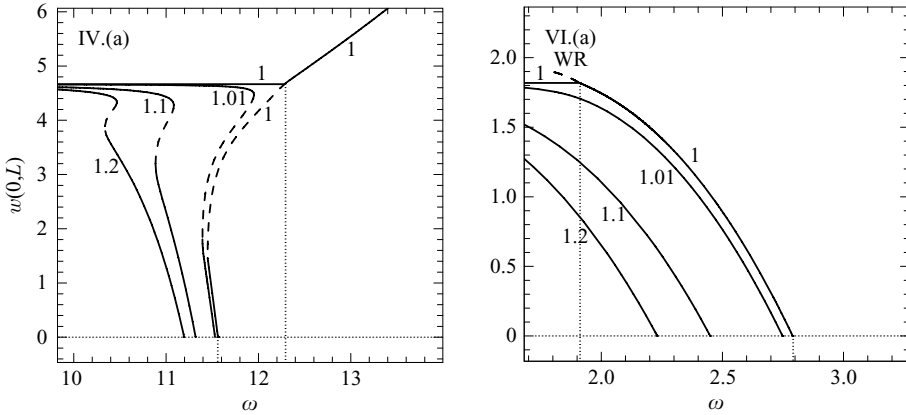


FIGURE 20. Bifurcation diagrams obtained for flows IV.(a) and VI.(a) in slightly diverging pipes of length  $L = 10$  and exit radii  $R(L) = 1, 1.01, 1.1$  and  $1.2$ . Solid lines denote stable flows and dashed lines denote unstable flows.

found for  $R(L) \leq 1.01$ , but note that we did not determine precisely the threshold in  $R(L)$  separating these two behaviours).

In case VI.(a), we find that irrespective of  $R(L)$ , all flows lie on a single stable branch. Consequently, as the inflow swirl is gradually increased, one will observe as expected columnar flows, then pre-breakdown flows, and finally breakdown flows, all being stable.

#### 4.3.4. Scenarios of transition to breakdown

Six types of bifurcation diagram have been found in § 4.3.2, depending on the inflow. Gathering their common points shows that three different scenarios of transition to breakdown may exist, including that of Wang & Rusak (1997a). To describe these scenarios, we extrapolate to a perturbed situation such as a very slight pipe divergence, as described in the previous paragraph; we refer the reader to Rusak & Meder (2004) or Leclaire *et al.* (2007b) for how to adapt these results in the case of a slight pipe convergence.

As the inlet swirl  $\omega$  is progressively increased from zero, one may obtain one of the following chains of events.

(a) Columnar flow for  $\omega < \omega_1$ , destabilization and abrupt transition to breakdown at  $\omega_1$  (I and IV).

(b) Columnar flow at low swirl, continuously evolving to breakdown, either via sinusoidal wave flows with  $\omega_R$  slightly larger than  $\omega_1$  (II and III), or via pre-breakdown flow with  $\omega_R > \omega_1$  (VI).

(c) Columnar flow for  $\omega < \omega_1$ , destabilization at  $\omega_1$ , abrupt transition to a pre-breakdown flow, continuous evolution towards breakdown for  $\omega_1 \leq \omega \leq \omega_R$  (V).

Conversely, starting at a swirl level where breakdown is observed (and large enough to have both  $\omega > \omega_R$  and  $\omega > \omega_1$ ) and decreasing it progressively, one may observe one of the following.

(a) Abrupt disappearance of breakdown at  $\omega = \omega_1$ , in favour of columnar flow that persists for  $\omega < \omega_1$  (I).

(b) Smooth transition from breakdown to columnar flow, via either sinusoidal wave (II and III) or pre-breakdown flows (VI).

(c) Smooth transition to a pre-breakdown flow, appearing for the first time either for  $\omega < \omega_1$  (IV) or for  $\omega > \omega_1$  (V), then disappearance of the pre-breakdown flow at  $\omega = \omega_2$ , in favour of the columnar flow.

Note that these conclusions are based on the properties of the decelerated branch that crosses the columnar branch at  $\omega_1$  and on the existence of the breakdown branch. It is not excluded that other steady flows may exist in the range of swirl numbers of interest here. In case I.(a) for instance, Mishra, Tadmor & Rusak (2008) recently found another steady and stable flow in the range  $\omega_0 < \omega < \omega_1$ , which, however, seems to be a less strong attractor than the breakdown flow, since it was not observed in the simulations of Rusak *et al.* (1998). This flow originates from a subsequent branching bifurcation from the columnar branch, for a swirl threshold  $\omega$  larger than  $\omega_1$ . We think that this is the only possibility for solutions to exist other than that reported in our study, since we did not observe branch crossing on the decelerated branches we computed.

## 5. Sensitivity analysis

We now return to the central question of the sensitivity of vortex breakdown onset to the upstream boundary conditions. We focus again on long pipes and base our analysis mainly on figures 12 and 19.

One of the most important conclusions of the present work is that plug axial flow with solid-body rotation should be viewed as a very specific inflow and represents a strong choice in a model. As shown in §4.3.2, its associated bifurcation diagrams are limit cases with a nearly vertical decelerated branch and involve no hysteresis whatever the third upstream boundary condition, which is a key difference with the more generic case of figure 1(a). In a more general way, figure 19 shows that weakly and strongly confined vortices (respectively large and small  $b$ ) may display very different nonlinear behaviours. In particular, there is almost no common point between a Burgers–Rott vortex and a rigidly rotating Poiseuille flow, the former obeying the scenario of loss of stability at  $\omega_1$  with hysteresis (I), and the latter being a theoretical limit of impossible vortex breakdown.

According to figure 19 and the bifurcation diagrams of §4.3.2, the sensitivity of vortex breakdown onset to the upstream boundary conditions (and conversely the degree of care to be taken for these conditions in a model) differs depending on the size of the rotational core. While for weakly confined vortices the switch between scenarios I and IV (and then V) occurs only for large values of  $d$ , i.e. strong axial jets, for solid-body rotation simply a small error on  $d$  may change the scenario from I to VI. Regarding the third upstream boundary condition, it has an influence on the transition scenario whenever scenarios IV, V or VI may arise. Firstly, this is because this condition may have an impact on the location of the separation lines between I, IV and V (as mentioned in §4.3.2). Secondly, this is because for each of the scenarios IV, V or VI, pre-breakdown is involved, so that different values of  $\omega_R$  are obtained depending on the choice for this condition, as shown by the diagrams of figure 15.

In the idea of modelling experiments as done in §2.2, this shows that swirl vane setups are very robust to a simplification of the upstream boundary conditions, while a rotating honeycomb requires the highest accuracy possible. For swirl vane setups, this may be understood by considering the dashed arrow in figures 12 and 19, which depicts the qualitative evolution of the upstream velocity profiles as  $\omega$  increases while the Reynolds number remains fixed, in a facility such as that of Faler & Leibovich (1978) or Mattner *et al.* (2002) (note that in the latter experiment, the rotational

core is even smaller, with  $b \approx 30$ ). As explained in §2.2, Faler & Leibovich (1978) related this progressive increase in  $d$  to an increase in the redistribution of momentum from the azimuthal towards the axial component. However in both these experiments, it was observed that the axial profiles remained in any case under the limit  $d < 1$ . Figures 12 and 19 thus confirm that modelling such setups with the Burgers–Rott vortex I ( $d = 0$  and  $b = 4$ ) is benign since during this evolution with  $\omega$ , the increase in  $d$  is not large enough for the switch towards IV to happen before the critical swirl  $\omega_1$  is reached. Both experiment and model indeed display the scenario I of appearance of breakdown following the destabilization of the columnar flow at  $\omega_1$ . As a result, the choice of the third upstream boundary condition should not be a matter of concern either, as long as breakdown does not settle directly downstream of the inlet. In the case of a rotating honeycomb, it is on the contrary crucial to precisely know the axial velocity for all swirl numbers, in order to discriminate between scenarios I (wakes), II (plug flow) and VI (jets). In the case of jets, the value of  $d$  should be known as precisely as possible since for  $d$  comprised between 0 (plug flow) and 2 (rigidly rotating Poiseuille flow),  $\omega_R$  may vary from  $\omega_1$  to  $+\infty$ . Besides, the third upstream boundary condition should be chosen as  $\psi_z(r, 0) = 0$ , consistent with the geometry of this setup, also in order to accurately predict  $\omega_R$  if case VI occurred.

More generally, these new scenarios raise the difficult question of how the experimental upstream boundary conditions may change in perturbed situations. This may arise as soon as  $\omega_1$  is reached. Indeed, except in the particular situations II and III, one observes either breakdown or pre-breakdown for  $\omega > \omega_1$  depending on the inflow, i.e. in both cases a perturbation that interacts with the inlet (see Rusak *et al.* 1998, for the case of breakdown). This question is in fact most acute for pre-breakdown, which appears only if the inflow axial velocity is a jet, whereas it precisely tends to transform the inflow into a wake. As rotating honeycombs seem to be better candidates than swirl vanes to observe such a flow, a crucial point is thus to determine if the progressive increase in  $d$  with  $\omega$  that we observed in our experiment (Leclaire *et al.* 2007a) is encountered in other facilities, and robust enough to persist beyond  $\omega_1$ . This is still an open question. As well as for the case of swirl vanes subjected to perturbations, further insight could be gained for instance by detailed measurements approaching as closely as possible the rotation-imparting device, or, in the same spirit as Snyder & Spall (2000)'s work, numerical simulations in which this device would be part of the calculated domain.

## 6. Conclusion

In this paper, we have investigated in a theoretical way how the currently accepted bifurcation structure leading to vortex breakdown in a pipe may change when the upstream boundary conditions are varied. This has been done by scanning a parameter space controlling the size of the inflow rotational core and the jet or wake character of its axial velocity, and allowing the third upstream boundary condition to be either a fixed azimuthal vorticity or a vanishing radial velocity.

In the most general case of long pipes, we have shown that including the classical configuration described by Wang & Rusak (1997a), where the decelerated flows have the form of a solitary wave, six bifurcation patterns may be encountered. Two of the new patterns involve flows akin to sinusoidal waves, comparable with that predicted by a weakly nonlinear analysis, and the other three involve new, fully nonlinear flows that we termed pre-breakdown. Contrary to solitary waves, both sinusoidal wave and pre-breakdown flows are linearly stable. Pre-breakdown consists of a perturbation

localized very close to the inlet, which realizes an axial transition between the inflow and a quasi-parallel flow characterized by an axial deceleration on the axis. It may first appear in the bifurcation diagrams for swirl levels lower or higher than the critical swirl, depending on the inflow profile.

In the inflow parameter space, the configuration of Wang & Rusak (1997a) is the most frequent and occurs for inflows with an axial profile of the wake or moderate jet type if the size of the rotational core remains moderate, and for very mild jets or wakes only if it is large or a solid-body rotation. Conversely, the three diagrams involving pre-breakdown flows are encountered for very strong jets if the rotational core is small or moderate, and mild jets or even any type of jet for large cores or solid-body rotation. Among these latter flows, our results have shown that the rigidly rotating Poiseuille flow appears as a singular limit for which vortex breakdown could be impossible, being predicted at infinitely large swirl numbers. The two diagrams involving sinusoidal wave flows occur only as very specific limit cases separating the two above scenarios, but remain theoretically important since they encompass plug axial flow with solid-body rotation.

Taking into account the common points of these bifurcation patterns, we found that by progressively increasing the inflow swirl level, three scenarios of transition to breakdown may be observed, including that of Wang & Rusak (1997a). In one of the new scenarios, the destabilization of the columnar flow at criticality first leads to a pre-breakdown flow and then to breakdown, while in the second a totally smooth transition to breakdown is observed, via sinusoidal wave or pre-breakdown flows. In both cases, the swirl of appearance of breakdown is larger than the critical swirl.

Our sensitivity analysis has shown that the degree of care to be taken when choosing upstream boundary conditions in a model consequently depends in the setup under consideration. While swirl vanes, which usually generate a weakly confined vortex, can be expected to lead to a very robust physics of vortex breakdown onset (except if they are able to generate a very strong axial jet), setups involving a rotating honeycomb should be modelled with care, as the wake or jet type of the axial profile directly determines the physics.

A natural perspective of this work is thus the more thorough investigation of very confined vortices and solid-body rotation, which have been shown to obey a different physics than traditionally accepted. Firstly, viscosity should be added to determine if actual rigidly rotating Poiseuille is indeed a limit flow in which vortex breakdown is impossible. Secondly, a no-slip condition at the wall should be considered instead of the present free-slip condition, in order to determine in what extent the new dynamics described here are also relevant for rotating honeycombs with a fixed pipe downstream. Both these ways of research should enable to understand in which conditions pre-breakdown flows may be observed experimentally, and more generally bring additional insights in the effect of radial confinement on vortex breakdown.

Laurent Jacquin is warmly acknowledged for inspiring this research. The authors also thank the referees for their comments and recommendations.

## **Appendix A. Numerical swirl thresholds for $L = 10$**

We here gather numerical data relative to the results of §4.3. Table 1 shows the values of the swirl thresholds associated with the bifurcation diagrams appearing in figures 14 and 15. The definition of each of these is recalled in the caption.

Case number		$d$	$b$	$\omega_1$	$\omega_2$	$\omega_R$	$\omega^*$	$\omega_R^{wnl}$
I.	(a)	0	4	3.534		3.154	2.834	3.077
	(b)	0	4	3.541		3.154		3.005
II.	(a)	0	0	1.9175		1.9175	1.9159	1.9175
	(b)	0	0	1.9223		1.9235		1.9234
III.	(a)	1.6263	1.6978	3.7926		3.7982	3.7967	3.7926
	(b)	1.6276	1.7042	3.8077		3.8162		3.8077
IV.	(a)	4.386	6	12.28	11.45	11.56	11.56	8.991
	(b)	4.386	6	12.29	11.45	11.73		8.423
V.	(a)	5.417	6	12.54	12.22	13.77	13.77	1.588
	(b)	5.417	6	12.55	12.22	14.45		$-3.949 \times 10^{-1}$
VI.	(a)	1.636	0	1.911		2.790	2.790	4.105
	(b)	1.636	0	1.914		3.173		4.525

TABLE 1. Definition of inflows I.(a)–VI.(b) and associated swirl thresholds,  $L = 10$ . (a)  $\psi_{zz}(r, 0) = 0$ , (b)  $\psi_z(r, 0) = 0$ . See (4.3) for the definition of parameters  $d$  and  $b$ .  $\omega_1$  is the critical swirl,  $\omega_R$  and  $\omega_R^{wnl}$  are the values for which  $w(0, L) = 0$  on the decelerated branch, obtained respectively by numerical continuation and the weakly nonlinear expansion of § 3.1.2.  $\omega_2$  is the swirl level of the turning point found on the decelerated branch, if any, and  $\omega^*$  is the swirl level for the turning point giving rise to the parallel breakdown solution (see § C.2).

## Appendix B. The Bragg–Hawthorne equation

In the literature, steady axisymmetric inviscid swirling flows are also investigated using the Bragg–Hawthorne equation (BHE)

$$\psi_{zz} + \psi_{rr} - \frac{\psi_r}{r} = r^2 H'(\psi) - K K'(\psi), \quad (\text{B } 1)$$

which is equivalent to the Squire–Long equations (2.2) with  $\partial/\partial t = 0$  (see, for instance, Batchelor 1967). Here  $H = p/\rho + (u^2 + v^2 + w^2)/2$  denotes the total head function, which only depends on  $\psi$  by virtue of Bernoulli’s first theorem. This equation is traditionally solved by prescribing boundary conditions (2.3)–(2.6), while functions  $H(\psi)$  and  $K(\psi)$  are determined thanks to (2.5) and (2.6) when this is analytically possible. In the same spirit as Buntine & Saffman (1995), our purpose here is to emphasize that flow analyses relying on this equation and on conserved quantities such as  $H$  and  $K$  are of help *only if the third upstream boundary condition is  $\psi_{zz}(r, 0) = 0$* , and not any more if  $\psi_z(r, 0) = 0$  is prescribed instead. As a matter of fact in the latter case, if several steady solutions exist at a same  $\omega$ , they may be characterized by different  $H'(\psi)$ , therefore different forms of the BHE. To see this, let us determine  $H$  for a given inflow. Using the projection of the momentum conservation along the radial direction, and denoting  $p_0 = p(0, 0)$  the pressure at the centre of the inlet plane, one obtains

$$H(r, 0) = \frac{p_0}{\rho} + \int_0^r \frac{v^2(r, 0)}{r} dr - \int_0^r w(r, 0) u_z(r, 0) dr + \frac{1}{2} (v^2(r, 0) + w^2(r, 0)). \quad (\text{B } 2)$$

If (2.6) is prescribed as the third upstream condition, then  $u_z(r, 0) = 0$  and  $H(r, 0)$  reduces to

$$H(r, 0) = \frac{p_0}{\rho} + \int_0^r \frac{v^2(r, 0)}{r} dr + \frac{1}{2}(v^2(r, 0) + w^2(r, 0)). \quad (\text{B } 3)$$

Since  $w(r, 0)$  and  $v(r, 0)$  are prescribed via (2.5), all flows at a given  $\omega$  are characterized by the same  $H_r(r, 0)$ . Thus, they also have the same  $H'(\psi)$ , since  $H'(\psi) = H_r(r, 0)/\psi_r(r, 0)$ , and  $\psi_r(r, 0)$  is prescribed via (2.5). On the contrary, when (2.7) is prescribed instead,  $u_z(r, 0)$  is a part of the solution and  $H(r, 0)$  is expressed as in (B 2); thus, flows at a swirl  $\omega$  may exhibit different  $H'(\psi)$ .

### Appendix C. Location of the bifurcation patterns in the $(d, b)$ plane

$(\psi_{zz}(r, 0) = 0, L = 10)$

This appendix explains the construction of figure 19, shown in §4.3.2, which delineates the zones of appearance of bifurcation diagrams I–VI in the  $(d, b)$  plane for  $L = 10$  and  $\psi_{zz}(r, 0) = 0$ .

#### C.1. Objective

In terms of geometry, the bifurcation diagrams plotted in figures 14 and 15 differ by

(a) the slope of the accelerated–decelerated branch at  $\omega = \omega_1$ , i.e. the sign of  $\mu$ : positive for I, IV and V, vanishing or nearly vanishing for II and III, and negative for VI;

(b) the slope of the decelerated branch at  $\omega = \omega_R$ : positive for I, and vanishing or negative for II–VI;

(c) the order of  $\omega_R$  and  $\omega_1$ , with in particular  $\omega_R < \omega_1$  for IV and  $\omega_R > \omega_1$  for V. Each bifurcation pattern found in §4.3.2 corresponds in fact to a different combination of these quantities, so that they can be used as detection criteria to determine the separation contours of figure 19.

While values of  $\mu$  for all possible inflows are readily obtained from our weakly nonlinear analysis (see §4.3.1), knowing the value of  $\omega_R$  and the corresponding orientation of the decelerated branch in the  $(d, b)$  plane for both choices of the third upstream boundary condition requires to run the numerical continuation for each given inflow, which is clearly excluded since it would lead to prohibitive computational times. We propose instead an approximate determination, valid only for  $\psi_{zz}(r, 0) = 0$ , which is described in the next paragraph.

#### C.2. Approximate determination of $\omega_R$ and the decelerated branch orientation at $\omega_R$

For this determination, we use the links that may be established between flows at the outlet of a finite-length pipe and *parallel* flows obtained for the same upstream boundary conditions (Wang & Rusak 1997a; Rusak *et al.* 1998), as explained below.

First, the parallel problem may be introduced by assuming that  $\psi_{zz}(r, 0) = 0$  so that the BHE (B 1) may be used. In fact, the axial position  $z = 0$  refers here more generally to an unperturbed zone located far upstream from the zone under consideration. Neglecting the term  $\psi_{zz}$  in this equation leads to

$$\psi_{rr} - \frac{\psi_r}{r} = r^2 H'(\psi) - K K'(\psi), \quad (\text{C } 1)$$

which has to be supplemented with adapted radial boundary conditions. In this paragraph, we will exclusively investigate flows with a central stagnation zone, and

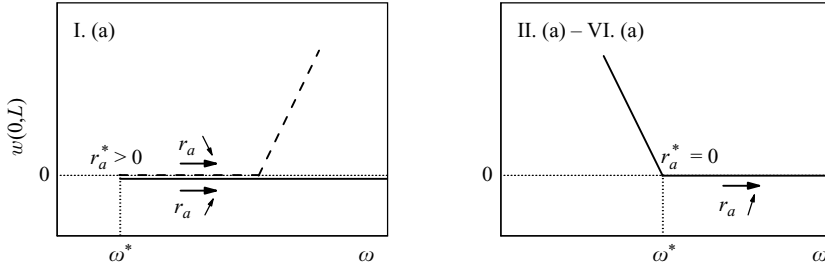


FIGURE 21. Link between the value of  $r_a^*$  and the sign of the slope of the decelerated branch at  $\omega = \omega_R$ .

thus consider

$$\psi(r_a) = 0, \quad (\text{C } 2a)$$

$$\psi_r(r_a) = 0, \quad (\text{C } 2b)$$

$$\psi(1) = q, \quad (\text{C } 2c)$$

where  $r_a$  denotes the radius of the stagnation zone, which is an unknown of the problem as in free-surface flows.

Wang & Rusak (1997a) have in particular studied this problem with a Burgers–Rott vortex at the inlet, i.e. in case I.(a). They have found that the bifurcation structure of the parallel problem is similar to that of the finite-length pipe, but with slightly smaller values of the swirl thresholds. Indeed, the key idea here is that parallel flows may be viewed as approximations of the flows in the outlet of a finite-length pipe, provided that the axial gradients there are weak. The small discrepancies observed by Wang & Rusak (1997a) were thus ascribed to the weak but not vanishing axial gradients at the outlet of the finite-length pipe. In particular, they have shown the existence of a turning point at a swirl level  $\omega = \omega^*$ , at which the parallel flow displays a central stagnation zone of finite radius  $r_a^*$ . This threshold is the analogous of  $\omega_0$  in a finite-length pipe (see figure 1a). As  $\omega$  increases from  $\omega^*$ , they have found that  $r_a$  decreases until it vanishes on one of the branches, and increases for the other. This situation is sketched in the left figure 21. Flows on the former branch may approximate the outlet states of the solitary wave flows (in the case of the finite-length pipe, a part of this branch indeed consists of flows with a central stagnation zone as shown again in figure 1a), while flows on the latter may approximate the outlet states of the breakdown flows. Thus, at a given  $\omega$ , if two flows with a central stagnation zone are found, breakdown is that with higher  $r_a$ .

In the present analysis, we investigated the parallel problem in the same way and found another possible configuration, sketched in the right figure 21, which prevails for inflows II.(a) to VI.(a). Technical details on this investigation are given in Appendix D. Starting at a swirl level high enough for a flow with a central stagnation zone to exist, we progressively decreased  $\omega$  until we attained a swirl level at which no solution with a stagnation zone may exist, which we defined as  $\omega^*$ . In any case, we also found that just prior to this disappearance, the radius of this stagnation zone vanishes, i.e.  $r_a^* = 0$ . Since for II.(a) to VI.(a), flows with incipient recirculation are indeed characterized by weak axial gradients at the outlet (see figures 16 and 17), one may infer that this branch organization is the same for the finite-length pipe problem, i.e. stable breakdown is the logical continuation of the decelerated branch for  $\omega > \omega_R$ . In particular, there is no turning point as for I.(a). This is confirmed by the agreement

between  $\omega^*$  and  $\omega_R$ , which is good for solitary wave flows (II.a and III.a) and excellent for pre-breakdown flows (IV.a to VI.a) as seen in table 1 in Appendix A.

With these conclusions in mind, the determination we look for is then readily obtained from  $r_a^*$  and  $\omega^*$ . As a matter of fact, as shown by figure 21,  $\omega^*$  may be considered a good approximation of  $\omega_R$  when  $r_a^* = 0$ , and in this case the decelerated branch has a negative slope at  $\omega_R$  (cases II–VI). Conversely, when  $r_a^* > 0$ , discrepancies exist between  $\omega^*$  and  $\omega_R$  and the decelerated branch has a positive slope at  $\omega_R$  (case I); note that in this case, these discrepancies are not impeding since it is not necessary to know  $\omega_R$  to distinguish between I and the other cases (see the previous paragraph).

As mentioned above, no such link between parallel and finite-length problem exists when  $\psi_z(r, 0) = 0$  is prescribed (b subcases) instead of  $\psi_{zz}(r, 0) = 0$ . However, seeing the diagrams II.(b)–VI.(b), it seems very probable to us that the same branch organization should be observed for these inflows.

### C.3. Results

In the same way as for  $\mu$  in the weakly nonlinear analysis, we calculated  $\omega^*$  and  $r_a^*$  for  $\psi_{zz}(r, 0) = 0$  in all the  $(d, b)$  plane. As explained above, this enabled us to know where in space one has  $r_a^* > 0$  (positive slope of the decelerated branch at  $\omega_R$ ) or  $r_a^* = 0$  (negative slope of the decelerated branch at  $\omega_R$ ), and in the latter case provided us with an approximation of  $\omega_R$ . We then plotted in the  $(d, b)$  plane the isolines  $\mu = 0$ ,  $\omega^* = \omega_1$  and the line separating  $r_a^* > 0$  and  $r_a^* = 0$ . For this latter line, we found that iso-value  $r_a^* = 0.01$  was an appropriate numerical limit to distinguish between both cases. Remembering the characterization of §C.1, this enabled us to locate the zone of appearance of all the bifurcation diagrams. This progressive construction and its outcome are sketched in figure 22.

Note that for this determination, we assumed that only diagrams I–VI were possible and thus focused only on the properties of the decelerated branch at  $\omega = \omega_1$  and  $\omega = \omega_R$ . This does not exclude the possibility of additional or different turning points on this branch; however, this would certainly require the existence of other new and more complex flow solutions, which we do not think very probable.

## Appendix D. Determination of $r_a^*$ and $\omega^*$ in the parallel problem ( $\psi_{zz}(r, 0) = 0$ )

### D.1. Principle

As mentioned above, to determine  $\omega^*$ , we follow the parallel breakdown branch in the direction of decreasing  $\omega$ . First, this requires to pick an initial  $\omega$  high enough for a flow with a central stagnation zone to exist. This is done by calculating  $\omega_B$  (which is the parallel analogous of  $\omega_1$ ; see §3.1.1), and then successively solving problem (C 1)–(C 2) for  $\omega = 0.5 \omega_B, \omega_B, 1.5 \omega_B \dots$  until a flow with  $r_a \neq 0$  is found. Details on the resolution of (C 1)–(C 2) at a fixed  $\omega$  are given in the next section. To ensure that the flow found is indeed the approximation of the outlet breakdown flows in situations where I prevails (see figure 21), we seek for  $r_a$  with a shooting method, by progressive decrements from the initial guess value  $r_a = 1$ . Since in case I, breakdown corresponds to the highest value of  $r_a$ , it will thus be the first solution encountered by our algorithm. Once this solution is found, we decrease  $\omega$  gradually, calculate the breakdown flow at each step, and finally obtain  $\omega^*$  when solutions with a stagnation zone disappear. The value of  $r_a^*$  is also recorded in the procedure. We validated this algorithm by ensuring that the same value of  $\omega^*$  for the Burgers–Rott vortex as in Rusak *et al.* (1998) was found.

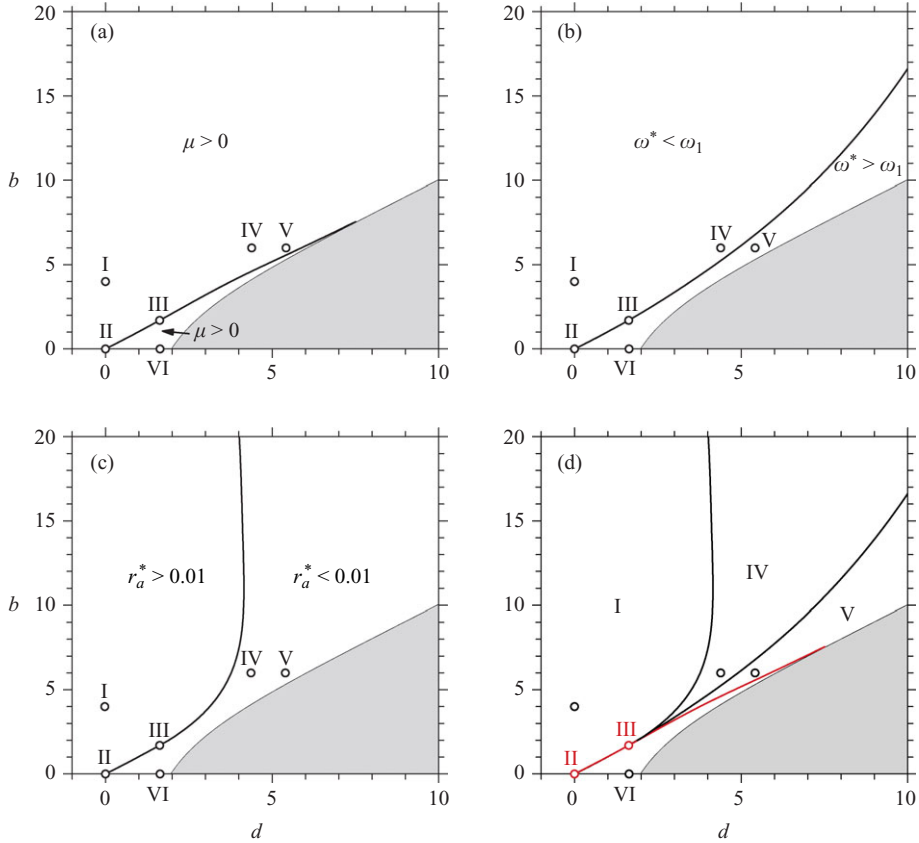


FIGURE 22. Location of the bifurcation diagrams in the  $(d, b)$  plane,  $\psi_{zz}(r, 0) = 0$  and  $L = 10$ . (Top left) location of positive and negative  $\mu$ . (Top right) zones corresponding to  $\omega^* < \omega_1$  and  $\omega^* > \omega_1$ . (Bottom left) zones corresponding to  $r_a^* > 0.01$  and  $r_a^* < 0.01$ . (Bottom right) location of the bifurcation diagrams, deduced from the other three subfigures.

### D.2. Numerical resolution of the BHE at a given $\omega$

With the present inflow profiles (4.1), it is not possible to analytically compute  $H(\psi)$  and  $K(\psi)$  as was the case in the study of Wang & Rusak (1997a). Here we can only explicitly determine  $\psi$  as a function of  $K$  i.e.  $\psi = f(K)$ , but this relation cannot be inverted analytically. We thus chose to numerically solve the parallel BHE (C 1) by writing it under the form

$$\psi_{rr} - \frac{\psi_r}{r} = \Lambda(K(\psi)), \quad (\text{D } 1)$$

where  $K(\psi)$  denotes the solution obtained by numerically inverting relation  $\psi = f(K)$ .

To do so, we introduce parameters

$$\alpha = 1 - \frac{d}{1 - e^{-b}}, \quad \beta = \frac{d}{2b} \frac{1}{1 - e^{-b}} \quad (\text{D } 2)$$

The inflow stream function is thus written as

$$\psi(r, 0) = \psi_0(r) = \alpha \frac{r^2}{2} + \beta \left(1 - e^{-br^2}\right). \quad (\text{D } 3)$$

We recall that its circulation  $K(r, 0)$  is given by

$$K(r, 0) = \omega K_0(r) = \frac{\omega}{b} \left(1 - e^{-br^2}\right). \quad (\text{D } 4)$$

Inverting this relation and considering  $r$  as a function of  $K(r, 0)$ , hereafter denoted by  $K$ , one gets

$$r = \left( \frac{\log \left(1 - \frac{bK}{\omega}\right)}{-b} \right)^{1/2}. \quad (\text{D } 5)$$

Replacing this into (D 3) thus yields the relation between  $\psi$  and  $K$  as

$$\psi = f(K) = -\frac{\alpha}{2b} \log \left(1 - \frac{bK}{\omega}\right) + \frac{\beta bK}{\omega}. \quad (\text{D } 6)$$

Introducing the  $K$ -dependence of  $H$  in the one-dimensional BHE (C 1) yields

$$\psi_{rr} - \frac{\psi_r}{r} = r^2 \left( \frac{dH}{dK} \frac{dK}{d\psi} \right) - K \frac{dK}{d\psi} = \frac{dK}{d\psi} \left( r^2 \frac{dH}{dK} - K \right). \quad (\text{D } 7)$$

From (D 6), one finds

$$\frac{dK}{d\psi} = \frac{2\omega(\omega - bK)}{\alpha\omega + 2\beta b(\omega - bK)}. \quad (\text{D } 8)$$

The value of the total head  $H$  as a function of  $K$  may also be calculated from the values at  $z=0$ . Indeed, denoting  $p_0 = p(0, 0)$  as in Appendix B, one has

$$H(r, 0) = \frac{p_0}{\rho} + \int_0^r \frac{v^2(r, 0)}{r} dr + \frac{1}{2}(v^2(r, 0) + w^2(r, 0)), \quad (\text{D } 9)$$

since  $\psi_{zz}(r, 0) = 0$  applies. This may be rewritten as

$$H(r, 0) = \frac{p_0}{\rho} + \int_0^r \frac{K^2(r, 0)}{r^3} dr + \frac{1}{2} \left( \frac{K^2(r, 0)}{r^2} + \frac{1}{r^2} \psi_{0r}^2(r, 0) \right). \quad (\text{D } 10)$$

Expressing again  $r$  as a function of  $K(r, 0)$ , denoted by  $K$ , one obtains

$$H(K) = \frac{p_0}{\rho} + \int_0^K \frac{1}{2} \frac{1}{\omega - bK} \frac{b^2 K^2}{\left(\log \left(1 - \frac{bK}{\omega}\right)\right)^2} dK + \frac{1}{2} \left[ \left( \alpha + 2\beta b \left(1 - \frac{bK}{\omega}\right) \right)^2 - \frac{bK^2}{\log \left(1 - \frac{bK}{\omega}\right)} \right] \quad (\text{D } 11)$$

and thus

$$\frac{dH}{dK} = -2\beta \frac{b^2}{\omega} \left( \alpha + 2\beta b \left(1 - \frac{bK}{\omega}\right) \right) - \frac{bK}{\log \left(1 - \frac{bK}{\omega}\right)}. \quad (\text{D } 12)$$

Finally, the one-dimensional BHE may be expressed as

$$\psi_{rr} - \frac{\psi_r}{r} = \Lambda(K) = \frac{-2\omega(\omega - bK)}{\alpha\omega + 2\beta b(\omega - bK)} \times \left[ K + r^2 \left[ 2\beta \frac{b^2}{\omega} \left( \alpha + 2\beta b \left( 1 - \frac{bK}{\omega} \right) \right) + \frac{bK}{\log \left( 1 - \frac{bK}{\omega} \right)} \right] \right]. \quad (\text{D } 13)$$

To solve this equation with boundary conditions (C2), we use a shooting method in  $r_a$ , starting from  $r_a = 1$ . For a given guess value, integration in  $r$  is performed with a Runge–Kutta scheme. For each value of  $\psi$ , the corresponding value of  $K$  is determined by solving (D6) by dichotomy.

#### REFERENCES

- ALTHAUS, W., BRUECKER, CH. & WEIMER, M. 1995 Breakdown of slender vortices. In *Fluid Vortices: Fluid Mechanics and Its Applications* (ed. S. I. Green), pp. 373–426. Kluwer.
- BATCHELOR, G. K. 1967 *An Introduction to Fluid Dynamics*. Cambridge University Press.
- BENJAMIN, T. B. 1962 Theory of the vortex breakdown phenomenon. *J. Fluid Mech.* **14**, 593–629.
- BERAN, P. S. & CULICK, F. E. C. 1992 The role of non-uniqueness in the development of vortex breakdown in tubes. *J. Fluid Mech.* **242**, 491–527.
- BILLANT, P., CHOMAZ, J.-M. & HUERRE, P. 1998 Experimental study of vortex breakdown in swirling jets. *J. Fluid Mech.* **376**, 183–219.
- BROWN, G. L. & LOPEZ, J. M. 1990 Axisymmetric vortex breakdown. II. Physical mechanisms. *J. Fluid Mech.* **221**, 553–576.
- BUNTINE, J. D. & SAFFMAN, P. G. 1995 Inviscid swirling flows and vortex breakdown. *Proc. R. Soc. Lond. A* **449**, 139–153.
- DELERY, J. 1994 Aspects of vortex breakdown. *Prog. Aerospace Sci.* **30**, 1–59.
- FALER, J. H. & LEIBOVICH, S. 1978 An experimental map of the internal structure of a vortex breakdown. *J. Fluid Mech.* **86**, 313–335.
- GALLAIRE, F. & CHOMAZ, J.-M. 2004 The role of boundary conditions in a simple model of incipient vortex breakdown. *Phys. Fluids* **16** (2), 274–286.
- GALLAIRE, F., CHOMAZ, J.-M. & HUERRE, P. 2004 Closed-loop control of vortex breakdown: a model study. *J. Fluid Mech.* **511**, 67–93.
- GOLDSHTIK, M. & HUSSAIN, F. 1997 The nature of inviscid vortex breakdown. *Phys. Fluids* **9**, 263.
- GOVAERTS, W. 2000 *Numerical Methods for Bifurcations of Dynamical Equilibria*. SIAM.
- GRABOWSKI, W. J. & BERGER, S. A. 1976 Solutions of the Navier–Stokes equations for vortex breakdown. *J. Fluid Mech.* **75**, 525–544.
- GRIMSHAW, R. 1990 Resonant flow of a rotating fluid past an obstacle: the general case. *Stud. Appl. Math.* **83**, 249–269.
- GRIMSHAW, R. & YI, Z. 1993 Resonant generation of finite-amplitude waves by the uniform flow of a uniformly rotating fluid past an obstacle. *Mathematika* **40**, 30–50.
- HAFEZ, M., KURUVILA, G. & SALAS, M. D. 1986 Numerical study of vortex breakdown. *Appl. Numer. Math.* **2** (3–5), 291–302.
- HANAZAKI, H. 1996 On the wave excitation and the formation of recirculation eddies in an axisymmetric flow of uniformly rotating fluids. *J. Fluid Mech.* **322**, 165–200.
- KELLER, H. B. 1977 Numerical solution of bifurcation and nonlinear eigenvalue problems. In *Applications of Bifurcation Theory*, pp. 359–384. Academic Press.
- KELLER, J. J., EGLI, W. & EXLEY, J. 1985 Force- and loss-free transitions between flow states. *J. Appl. Math. Phys.* **36**, 854–889.
- KOPECKY, R. M. & TORRANCE, K. E. 1973 Initiation and structure of axisymmetric eddies in a rotating stream. *Comput. Fluids* **1**, 289–300.
- KUZNETSOV, Y. A. 2004 *Elements of Applied Bifurcation Theory*. Springer.

- LECLAIRE, B., JACQUIN, L. & SIPP, D. 2007a The generating conditions of a high-Reynolds-number swirling jet. In *Fifth Turbulence and Shear Flow Phenomena Sympos., Munich, Germany, August 27–29*.
- LECLAIRE, B., SIPP, D. & JACQUIN, L. 2007b Near-critical swirling flow in a contracting duct: the case of plug axial flow with solid-body rotation. *Phys. Fluids* **19** (9), 091701.
- LEIBOVICH, S. 1984 Vortex stability and breakdown: survey and extension. *AIAA J.* **22** (9), 1192–1206.
- LEIBOVICH, S. & KRIBUS, A. 1990 Large-amplitude wavetrains and solitary waves in vortices. *J. Fluid Mech.* **216**, 459–504.
- LIANG, H. & MAXWORTHY, T. 2005 An experimental investigation of swirling jets. *J. Fluid Mech.* **525**, 115–159.
- LOPEZ, J. M. 1994 On the bifurcation structure of axisymmetric vortex breakdown in a constricted pipe. *Phys. Fluids* **6** (11), 3683–3693.
- LUCCA-NEGRO, O. & O'DOHERTY, T. 2001 Vortex breakdown: a review. *Progr. Energy Combust. Sci.* **27** (4), 431–481.
- MATTNER, T. W., JOUBERT, P. N. & CHONG, M. S. 2002 Vortical flow. part 1. flow through a constant-diameter pipe. *J. Fluid Mech.* **463**, 259–291.
- MISHRA, A., TADMOR, G. & RUSAK, Z. 2008 On the dynamics of axisymmetric vortex breakdown in a pipe. In *Fifth AIAA Theoretical Fluid Mechanics Conf., Seattle, WA, June 23–26*.
- PECKHAM, D. H. & ATKINSON, S. A. 1957 Preliminary results of low speed wind tunnel tests on a gothic wing of aspect ratio 1.0. *ARC Tech. Rep. CP-508*.
- RAYLEIGH, LORD 1916 On the dynamics of revolving fluids. *Proc. R. Soc. Lond. A* **93**, 148–154.
- RUSAK, Z. 1998 The interaction of near-critical swirling flows in a pipe with inlet azimuthal vorticity perturbations. *Phys. Fluids* **10** (7), 1672–1684.
- RUSAK, Z. & JUDD, K. P. 2001 The stability of noncolumnar swirling flows in diverging streamtubes. *Phys. Fluids* **13** (10), 2835–2844.
- RUSAK, Z., JUDD, K. P. & WANG, S. 1997 The effect of small pipe divergence on near-critical swirling flows. *Phys. Fluids* **9** (8), 2273–2285.
- RUSAK, Z. & MEDER, C. C. 2004 Near-critical swirling flow in a slightly contracting pipe. *AIAA J.* **42** (11), 2284–2293.
- RUSAK, Z., WANG, S. & WHITING, C. H. 1998 The evolution of a perturbed vortex in a pipe to axisymmetric vortex breakdown. *J. Fluid Mech.* **366**, 211–237.
- SALAS, M. D. & KURUVILA, G. 1989 Vortex breakdown simulation: a circumspect study of the steady, laminar, axisymmetric model. *Comput. Fluids* **17** (1), 247–262.
- SARPKAYA, T. 1971 On stationary and travelling vortex breakdowns. *J. Fluid Mech.* **45**, 545–559.
- SARPKAYA, T. 1995 Turbulent vortex breakdown. *Phys. Fluids* **7** (10), 2301–2303.
- SNYDER, D. O. & SPALL, R. E. 2000 Numerical simulation of bubble-type vortex breakdown within a tube-and-vane apparatus. *Phys. Fluids* **12** (3), 603–608.
- SQUIRE, H. B. 1960 Analysis of the vortex breakdown phenomenon, part I. *Imperial College, Aero. Dept. Rep.* **102**.
- WANG, S. & RUSAK, Z. 1996a On the stability of an axisymmetric rotating flow in a pipe. *Phys. Fluids* **8** (4), 1007–1016.
- WANG, S. & RUSAK, Z. 1996b On the stability of non-columnar swirling flows. *Phys. Fluids* **8** (4), 1017–1023.
- WANG, S. & RUSAK, Z. 1997a The dynamics of a swirling flow in a pipe and transition to axisymmetric vortex breakdown. *J. Fluid Mech.* **340**, 177–223.
- WANG, S. & RUSAK, Z. 1997b The effect of slight viscosity on a near-critical swirling flow in a pipe. *Phys. Fluids* **9** (7), 1914–1927.